The Astrophysical Journal, 908:88 (19pp), 2021 February 10 https://doi.org/10.3847/1538-4357/abd3a6

Two-dimensional Particle-in-cell Simulations of Axisymmetric Black Hole Magnetospheres

Kouichi Hirotani[1], Ruben Krasnopolsky[1], Hsien Shang (尚賢)[1], Ken-ichi Nishikawa[2], and Michael Watson[3,4]
[1] Institute of Astronomy and Astrophysics, Academia Sinica, Taipei 10617, Taiwan, Republic of China; hirotani@asiaa.sinica.edu.tw, shang@asiaa.sinica.edu.tw
[2] Department of Physics, Chemistry and Mathematics, Alabama A&M University, Huntsville, AL 35811, USA
[3] Department of Physics, Fisk University, 1000 17th Avenue North, Nashville, TN 37208, USA
[4] University Park Dr, Nashville, TN 37204, USA
Received 2020 July 22; revised 2020 November 26; accepted 2020 December 13; published 2021 February 16

Abstract

We investigate the temporal evolution of an axisymmetric magnetosphere around a rapidly rotating stellar-mass black hole by applying a two-dimensional particle-in-cell simulation scheme. Adopting homogeneous pair production and assuming that the mass accretion rate is much less than the Eddington limit, we find that the black hole's rotational energy is preferentially extracted from the middle latitudes and that this outward energy flux exhibits an enhancement that lasts approximately 160 dynamical timescales. It is demonstrated that the magnetohydrodynamic approximations cannot be justified in such a magnetically dominated magnetosphere because Ohm's law completely breaks down and the charge-separated electron–positron plasmas are highly nonneutral. An implication is given regarding the collimation of relativistic jets.

Unified Astronomy Thesaurus concepts: Kerr black holes (886); Astronomical simulations (1857); Stellar magnetic fields (1610); General relativity (641)

1. Introduction

It is commonly accepted that every active galaxy harbors a supermassive black hole (BH) in its center (Ferrarese et al. 1996; Kormendy & Ho 2013; Larkin & McLaughlin 2016). A likely mechanism for powering their relativistic jets is the release of the rotational energy of the BHs (Blandford & Znajek 1977), which is referred to as the Blandford–Znajek (BZ) process, as demonstrated by general-relativistic (GR) magnetohydrodynamic (MHD) simulations (Koide et al. 2002; McKinney et al. 2012). In the polar region of a BH magnetosphere, centrifugal force prevents accretion toward the rotation axis, and a high vacuum is maintained (Hirose et al. 2004). In this nearly vacuum BH magnetosphere, electrons and positrons ($e^{\pm}$) are supplied via the collisions of MeV photons emitted from the equatorial, advection-dominated accretion flow (ADAF; Ichimaru 1977; Narayan & Yi 1994). Particularly, when the mass accretion rate is much less than the Eddington rate, the collisions can no longer sustain a force-free magnetosphere (Levinson & Rieger 2011). In such a charge-starved magnetosphere, an electric field appears along the magnetic field lines. In this vacuum gap, a portion of the BZ flux is dissipated as particle acceleration and radiation (Beskin et al. 1992; Hirotani & Okamoto 1998; Neronov & Aharonian 2007; Hirotani & Pu 2016). Such a highly vacuum BH magnetosphere has been investigated by the particle-in-cell (PIC) scheme one-dimensionally along a radial magnetic field line (Chen et al. 2018; Levinson & Cerutti 2018; Chen & Yuan 2020; Kisaka et al. 2020) and two-dimensionally in the poloidal plane (Parfrey et al. 2019; Crinquand et al. 2020). In the present paper, by adopting a fixed magnetic field in the poloidal plane, we perform a two-dimensional (2D), axisymmetric PIC simulation around a stellar-mass BH. We will examine the temporal evolution of the poloidal components of the electric field, the toroidal component of the magnetic field, and the distribution functions of the electrons and positrons that are created and accelerated within the BH magnetosphere.

After describing the background spacetime in Section 2.1, we consider the initial conditions of the PIC simulation in Section 2. Then we present the results of our 2D GR PIC simulation in Section 3, demonstrating that the MHD approximations totally break down in the vicinity (i.e., at the jet-launching region) of rotating BHs that accrete plasmas at a much lower rate than the Eddington rate. In the present paper, we focus on a set of astrophysical cases, as described in Section 3.5. Code testing cases, including comparison with exact solutions (e.g., development of the electromagnetic field in a plasma-free spacetime or propagations of charged particles in a fixed electromagnetic field), have been performed but will be deferred to subsequent papers. Finally, in Section 4, we discuss the implication of astrophysical applications to the very long baseline interferometric (VLBI) observations of supermassive BHs in the center of low-luminosity active galactic nuclei.

2. Stationary Magnetosphere

Let us begin with the stationary solution of the electromagnetic fields in a magnetosphere of a rotating BH. We will use this stationary solution as the initial condition of time-dependent PIC simulations. Throughout the present paper, we consider a 2D structure of the BH magnetosphere in which electrons and positrons are created and accelerated, assuming axisymmetry with respect to the rotation axis of the BH.

2.1. Background Geometry

Around a rotating, noncharged BH, the background geometry is described by the Kerr metric (Bardeen 1970). In the Boyer–Lindquist coordinates (Boyer & Lindquist 1967), the line element can be expressed as

$$ds^2 = g_{tt}dt^2 + 2g_{t\varphi}dtd\varphi + g_{\varphi\varphi}d\varphi^2 + g_{rr}dr^2 + g_{\theta\theta}d\theta^2, \quad (1)$$

where

$$g_{tt} \equiv -\frac{\Delta - a^2\sin^2\theta}{\Sigma}, \qquad g_{t\varphi} \equiv -\frac{2Mar\sin^2\theta}{\Sigma}, \quad (2)$$

$$g_{\varphi\varphi} \equiv \frac{A\sin^2\theta}{\Sigma}, \qquad g_{rr} \equiv \frac{\Sigma}{\Delta}, \qquad g_{\theta\theta} \equiv \Sigma; \tag{3}$$

$\Delta \equiv r^2 - 2Mr + a^2$, $\Sigma \equiv r^2 + a^2\cos^2\theta$, $A \equiv (r^2+a^2)^2 - \Delta a^2\sin^2\theta$. In Equations (1)–(3), we adopt the geometrized unit, putting $c = G = 1$, where c and G denote the speed of light and the gravitational constant. The horizon radius, $r_{\rm H} \equiv M + \sqrt{M^2 - a^2}$, is obtained by $\Delta = 0$, where M corresponds to the gravitational radius. The spin parameter becomes $a = M$ for a maximally rotating BH and $a = 0$ for a nonrotating BH.

2.2. The Zero Angular Momentum Observer

As a fiducial observer, let us introduce the zero angular momentum observer (ZAMO), who is static in the poloidal plane (r, θ) but rotates around the BH at the same angular frequency as the spacetime frame-dragging frequency, $\omega \equiv -g_{t\varphi}/g_{\varphi\varphi}$. The tetrad of the ZAMO reads

$$\tilde{\boldsymbol{e}}_{(\hat{t})} = \alpha^{-1}(\tilde{\boldsymbol{e}}_{(t)} + \omega\tilde{\boldsymbol{e}}_{(\varphi)}), \tag{4}$$

$$\tilde{\boldsymbol{e}}_{(\hat{r})} = \sqrt{\frac{\Delta}{\Sigma}}\tilde{\boldsymbol{e}}_{(r)}, \tag{5}$$

$$\tilde{\boldsymbol{e}}_{(\hat{\theta})} = \frac{1}{\sqrt{\Sigma}}\tilde{\boldsymbol{e}}_{(\theta)}, \tag{6}$$

$$\tilde{\boldsymbol{e}}_{(\hat{\varphi})} = \frac{1}{\sqrt{g_{\varphi\varphi}}}\tilde{\boldsymbol{e}}_{(\varphi)}, \tag{7}$$

where

$$\alpha \equiv \frac{d\tau}{dt} = \frac{\rho_{\rm w}}{\sqrt{g_{\varphi\varphi}}} = \sqrt{\frac{\Delta\Sigma}{A}} \tag{8}$$

denotes the lapse; $d\tau$ refers to the ZAMO proper time. The tilde (~) represents a ZAMO-measured quantity, and the caret (^) shows that the component is projected on an orthonormal basis. At the horizon, we have $\alpha = 0$, while away from the BH, we have $\alpha = 1$. The coordinate bases are defined as

$$\boldsymbol{e}_{(t)} = \partial_t, \quad \boldsymbol{e}_{(r)} = \partial_r, \quad \boldsymbol{e}_{(\theta)} = \partial_\theta, \quad \boldsymbol{e}_{(\varphi)} = \partial_\varphi. \tag{9}$$

We use the ZAMO to solve the electromagnetic fields in a stationary magnetosphere (Section 2.3), as well as to present the current densities (Figures 8 and 9) and the particle distribution functions (Figures 10 and 11) in a nonstationary magnetosphere (Section 3).

2.3. Gauss's and Biot–Savart Laws

To describe the stationary electromagnetic field, we should simultaneously solve Gauss's law and the Biot–Savart law. The expressions of these two laws are derived in Appendix B. For convenience, we replace the independent variable r with the so-called "tortoise coordinate," r_*. It is defined by

$$\frac{dr_*}{dr} = \frac{r^2 + a^2}{\Delta}. \tag{10}$$

In this coordinate, the horizon corresponds to $r_* \to -\infty$. At large distances, $dr_*/dr \to 1$.

What is more, to avoid the singular behavior due to the $\csc\theta$ factors in Gauss's law (Equation (B17)) and the Biot–Savart law (Equation (B19)) at the poles (i.e., at $\theta = 0$ and π), we introduce a new meridional variable, $y \equiv 1 - \cos\theta$. Adopting this y coordinate, we obtain

$$\frac{1}{\sin\theta}\frac{\partial}{\partial\theta} = \frac{\partial}{\partial y}. \tag{11}$$

To avoid the change of the type of the second-order partial differential equation (specifically, the Biot–Savart law) at the static limit, we replace the electrostatic potential A_t with the ZAMO-measured value $A_{\hat{t}}$. The tetrad of the ZAMO (Equations (4)–(7)) gives

$$A_t = \alpha A_{\hat{t}} - \omega A_\varphi \tag{12}$$

and

$$A_\varphi = \sqrt{g_{\varphi\varphi}}A_{\hat{\varphi}}. \tag{13}$$

Using $A_{\hat{t}}$, A_φ, r_*, and y, the Biot–Savart law (Equation (B19)) can be rewritten as

$$\begin{aligned}
&-\frac{\Delta\Sigma}{A}\frac{\partial^2 A_\varphi}{\partial {r_*}^2} + C_1\frac{\partial A_\varphi}{\partial r_*} - \frac{\Delta^2\Sigma\sin^2\theta}{(r^2+a^2)^2 A}\frac{\partial^2 A_\varphi}{\partial y^2} \\
&+ \left(\frac{\Delta}{r^2+a^2}\right)^2\frac{4Ma^2 r\sin^2\theta\cos\theta}{\Sigma A}\frac{\partial A_\varphi}{\partial y} + C_0 A_\varphi \\
&+ \frac{2Mar\sin^2\theta}{\Sigma}\frac{\partial^2}{\partial {r_*}^2}(\alpha A_{\hat{t}}) + C_2\frac{\partial}{\partial r_*}(\alpha A_{\hat{t}}) \\
&+ \frac{2Mar\Delta\sin^2\theta}{(r^2+a^2)^2\Sigma}\frac{\partial^2}{\partial y^2}(\alpha A_{\hat{t}}) \\
&+ \frac{4Mar\Delta\sin^2\theta\cos\theta}{(r^2+a^2)\Sigma^2}\frac{\partial}{\partial y}(\alpha A_{\hat{t}}) \\
&= 4\pi\left(\frac{\Delta}{r^2+a^2}\right)^2\Sigma\sin^2\theta\cdot J^\varphi,
\end{aligned} \tag{14}$$

where

$$\begin{aligned}
C_0 \equiv &-\frac{2Mar\Delta\sin^2\theta}{(r^2+a^2)^2\Sigma}\{\Delta(\partial_r{}^2\omega) \\
&+ \left[\frac{(r^2 - a^2\cos^2\theta)\Delta}{r\Sigma} - \frac{2M(r^2-a^2)}{r^2+a^2}\right](\partial_r\omega) \\
&+ \sin^2\theta(\partial_y{}^2\omega) \\
&+ \frac{2(r^2+a^2)\cos\theta}{\Sigma}(\partial_y\omega)\Big\},
\end{aligned} \tag{15}$$

$$\begin{aligned}
C_1 \equiv &\frac{2\Delta}{(r^2+a^2)^2\Sigma^2} \\
&\times [-(r-M)(r^2+a^2)\Sigma + \frac{(r^2+a^2)\Sigma}{A}C_3 \\
&+ (\Delta - a^2\sin^2\theta)ra^2\sin^2\theta + \frac{4M^2a^4r^3\sin^4\theta}{A} \\
&+ 2Mar\sin^2\theta(r^2+a^2)\Sigma(\partial_r\omega)],
\end{aligned} \tag{16}$$

$$\begin{aligned}
C_2 \equiv &\frac{2Ma\sin^2\theta}{(r^2+a^2)^2\Sigma^2} \\
&\times [-r^6 + a^2(-2+\cos^2\theta)r^4 + 4Ma^2\sin^2\theta r^3 \\
&+ a^4(1-2\sin^2\theta)r^2 + a^6\cos^2\theta],
\end{aligned} \tag{17}$$

$$C_3 \equiv (r - M)A + a^2 \sin^2\theta \times [-r^3 - 3Mr^2 + (2M^2 - a^2\cos^2\theta)r + a^2 M \cos^2\theta]. \quad (18)$$

It follows that the four highest-order derivative terms of Equation (14) have definite signs; thus, the Biot–Savart law now becomes an elliptic type in the entire simulation region because we adopt a physical observer: the ZAMO.

Gauss's law (Equation (B17)) can also be rewritten with respect to $\alpha A_{\hat{t}}$ and A_φ. Multiplying $[\Delta/(r^2 + a^2)]^2$ on both sides, we obtain

$$\frac{A}{\Sigma^2}\frac{\partial^2(\alpha A_{\hat{t}})}{\partial r_*^2} + D_1\frac{\partial(\alpha A_{\hat{t}})}{\partial r_*} - \frac{\Delta A}{(r^2+a^2)\Sigma^2}(\partial_r\omega)\frac{\partial A_\varphi}{\partial r_*} + \frac{\Delta A\sin^2\theta}{(r^2+a^2)^2\Sigma^2}\frac{\partial^2(\alpha A_{\hat{t}})}{\partial\xi^2} + \frac{2\Delta\cos\theta}{(r^2+a^2)^2\Sigma^3}[(r^2+a^2)A - a^2\Delta\Sigma\sin^2\theta]\frac{\partial(\alpha A_{\hat{t}})}{\partial\xi} + \frac{2\Delta\sin^2\theta}{(r^2+a^2)^2\Sigma^2}[-A(\partial_\xi\omega) + \Delta a^2\cos\theta\cdot\omega]\frac{\partial A_\varphi}{\partial\xi} + D_0 A_\varphi = 4\pi\rho\left(\frac{\Delta}{r^2+a^2}\right)^2, \quad (19)$$

where

$$D_0 \equiv \frac{\Delta A}{(r^2+a^2)^2\Sigma^2}\left\{-\Delta(\partial_r{}^2\omega) - \sin^2\theta(\partial_\xi{}^2\omega) + \left[2(r-M) - \Delta\partial_r\left(\ln\frac{\Delta A}{\Sigma}\right)\right](\partial_r\omega) - \frac{2\cos\theta}{\Sigma}\left[r^2 + a^2 - \frac{\Delta\Sigma}{A}a^2\sin^2\theta\right](\partial_\xi\omega)\right\} \quad (20)$$

and

$$D_1 \equiv -\frac{A}{(r^2+a^2)\Sigma^2} \times \left[2(r-M) - \Delta\partial_r\left(\ln\frac{(r^2+a^2)A}{\Sigma}\right)\right]. \quad (21)$$

Note that the $\partial^2 A_\varphi/\partial r_*^2$ and $\partial^2 A_\varphi/\partial\xi^2$ terms vanish in Equation (19).

2.4. Boundary Conditions

We search for the stationary solution that satisfies Gauss's law (Equation (19)) and the Biot–Savart law (Equation (14)). To this end, we must impose boundary conditions on $\alpha A_{\hat{t}}$ and A_φ or, equivalently, on A_t and A_φ. In the present paper, we solve these two equations in the first and fourth quadrants of the poloidal plane (r, θ). The region is bordered by

1. the polar boundaries at $\theta = 0$ (north polar axis) and $\theta = \pi$ (south polar axis),
2. the inner boundary at $r = r_{\rm H}$, and
3. the outer boundary at $r = r_{\rm out}$, where $r_{\rm out} \gg r_{\rm g} \equiv GMc^{-2} = M$.

In this subsection, we describe the boundary conditions at these three boundaries.

At the northern and southern polar boundaries, we impose $E_\theta = \partial_\theta A_t = 0$, that is, a Neumann condition on A_t. We also impose $B^\theta \propto F_{\varphi r} = -\partial_r A_\varphi = 0$. Thus, we put $A_\varphi = 0$ at $\theta = 0$ and π and measure the magnetic flux function A_φ from the rotation axis.

At the inner boundary, we impose $\boldsymbol{E}\cdot\boldsymbol{B} = 0$ and $F_{\varphi r} = 0$, where $F^{r\theta} = 0$ is assumed at $t = 0$. For instance, in the ZAMO, these conditions constrain that both the radial component of the electric field and the meridional component of the magnetic field vanish at the inner boundary.

At the outer boundary ($r = r_{\rm out} \gg M$), we impose $\boldsymbol{E}\cdot\boldsymbol{B} \propto (\partial_r A_t)(\partial_\theta A_\varphi) - (\partial_\theta A_t)(\partial_r A_\varphi) = 0$ and $\partial_r A_\varphi = 0$, the latter of which comes from the assumption of a split-monopole magnetic field, $J^\varphi_{\rm eq} \propto r^{-4}$. Thus, in the present paper, we impose the Neumann condition, $\partial_r A_t = 0$. However, in general, if we impose the magnetic field direction, $\partial_r A_\varphi/\partial_\theta A_\varphi$ (e.g., if we adopt a paraboloidal magnetic field; Blandford & Znajek 1977, hereafter BZ77), $\boldsymbol{E}\cdot\boldsymbol{B} = 0$ constrains the direction of the A_t = constant surface at the outer boundary.

2.5. Disk Toroidal Current

We assume that the plasmas in an ADAF produce a toroidal current $J^\varphi_{\rm eq} = C_{\rm eq} r^{-4}$ near the equator all the way to the horizon within the colatitudes $87° < \theta < 93°$; outside of this equatorial region, $J^\varphi_{\rm eq} = 0$ is assumed. For a slowly rotating BH, this disk current produces a split-monopole magnetic field (BZ77).

The normalization factor $C_{\rm eq}$ is adjusted so that the meridionally averaged, ZAMO-measured radial magnetic field strength at $r = 2M$,

$$\langle B^r(2M)\rangle \equiv \frac{\int_0^\pi \tilde{B}^{\hat{r}}(2M,\theta)\sqrt{A}\sin\theta d\theta}{\int_0^\pi \sqrt{A}\sin\theta d\theta}, \quad (22)$$

may match a fraction of the equipartition field strength (Yuan & Narayan 2014),

$$B_{\rm eq}(r) = 9.7\times 10^7\left(\frac{\dot{m}}{M_1}\right)^{1/2}\left(\frac{r}{2M}\right)^{-5/4}\ {\rm G}, \quad (23)$$

which is obtained if there is an equipartition between the magnetic field energy density and the plasma internal energy density; the alpha viscous parameter is assumed to be 0.3. The dimensionless accretion rate $\dot{m}$ is defined by

$$\dot{m} \equiv \frac{\dot{M}}{\dot{M}_{\rm Edd}}, \quad (24)$$

where $\dot{M}$ denotes the mass accretion rate. The Eddington accretion rate is defined by

$$\dot{M}_{\rm Edd} \equiv \frac{L_{\rm Edd}}{\eta_{\rm eff}c^2} = 1.39\times 10^{19} M_1\ {\rm g\ s^{-1}}, \quad (25)$$

where $L_{\rm Edd}$ denotes the Eddington luminosity; the conversion efficiency is assumed to be $\eta_{\rm eff} = 0.1$.

In the present paper, we adopt a relatively small mass accretion rate, $\dot{m} = 2.25\times 10^{-4}$, and $\langle B^r(2M)\rangle = B_{\rm eq}(2M)$.

2.6. Stationary Solution

In the present paper, we consider a 10 $M_\odot$ BH, $M_1 \equiv M/(10\,M_\odot) = 1$, and solve Equations (14) and (19) iteratively in

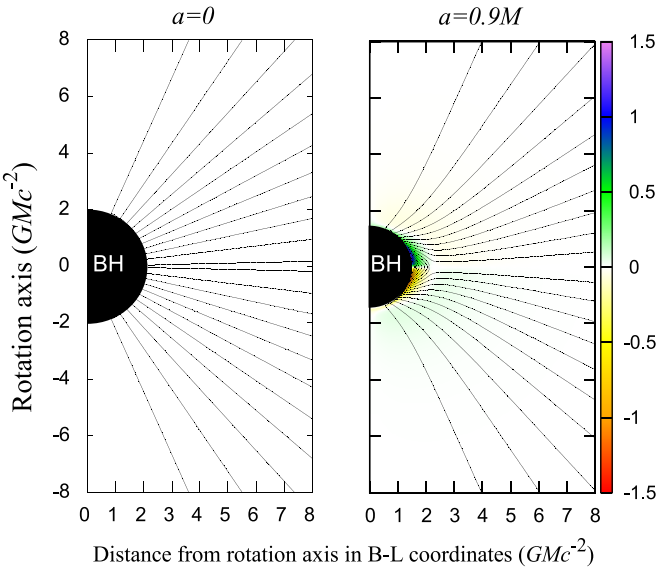

Figure 1. Stationary equi-A_φ contours (solid black curves) and the distribution of $\boldsymbol{E}\cdot\boldsymbol{B}/B_{\rm eq}(2M)^2$ (color) on the poloidal plane $(r,\,\theta)$. The equatorial current density is assumed to depend on r as $J^\varphi_{\rm eq}\propto r^{-4}$. The ordinate represents the distance along the rotational axis of the BH, while the abscissa represents the distance $r\sin\theta$ from the rotation axis. Both axes show lengths in the Boyer–Lindquist coordinates normalized by the gravitational radius, $r_{\rm g}=GMc^{-2}=M$. The equatorial plane corresponds to the ordinate of zero. The black filled circle shows the BH. The left panel shows the equi-A_φ contours when $a=0$, in which case the solid curves denote the magnetic field lines measured by a distant static observer. For $a=0$, no electric fields arise along the magnetic field lines; thus, the background color is entirely white. The right panel shows the case of $a=0.9M$. The amplitude of $\boldsymbol{E}\cdot\boldsymbol{B}$ increases with increasing a because the frame-dragging effect increases with increasing BH spin, a.

the region $r_{\rm H}<r\leqslant 20M$ and $0\leqslant\theta\leqslant\pi$. The solved electromagnetic fields are presented in Figure 1. In each panel, solid black curves show the equi-A_φ contours, which indicate the poloidal magnetic field lines for a distant static observer if $a=0$. We superpose $\boldsymbol{E}\cdot\boldsymbol{B}/[B_{\rm eq}(r=2M)]^2$, whose values are indicated in the color code. The left and right panels correspond to the cases of $a=0$ and $0.9M$, respectively.

In the left panel, $\boldsymbol{E}\cdot\boldsymbol{B}=0$ holds everywhere; thus, the background color is entirely white. It follows that the poloidal magnetic field becomes radial for a slowly rotating BH when $J^\varphi_{\rm eq}\propto r^{-4}$, which is consistent with the analytical conclusion (Blandford & Znajek 1977; McKinney & Narayan 2007). Because of $a=0$, there is no magnetic field–aligned electric field, $E_\parallel$; thus, A_φ is solved only from the Biot–Savart law.

However, as the BH spins up (i.e., if $a\neq 0$), the right panel shows that a nonvanishing $E_\parallel$ arises due to the relative rotational motion of the magnetic field lines with respect to the spacetime. At the same time, the equi-A_φ lines deviate from a radial shape, as the solid curves indicate. For a rapidly rotating case, $a=0.9M$, the magnetic field lines are laterally pushed toward the rotation axis in the ergosphere (Tanabe & Nagataki 2008; Tchekhovskoy et al. 2010). Note that the magnetosphere is assumed to be a vacuum in the present analysis, while it is force-free (i.e., plasma-filled) in Blandford & Znajek (1977), Tanabe & Nagataki (2008), and Tchekhovskoy et al. (2010). To examine how the magnetic field lines are actually deformed for a physical observer, we adopt the ZAMO and plot in Figure 2 the radial ($\tilde{B}^{\hat{r}}$; left panel) and meridional ($\tilde{B}^{\hat{\theta}}$; right panel) components of the magnetic field, where their explicit expressions are given by Equations (A12) and (A13). It shows that $|\tilde{B}^{\hat{\theta}}|$ is kept below $|\tilde{B}^{\hat{r}}|$,

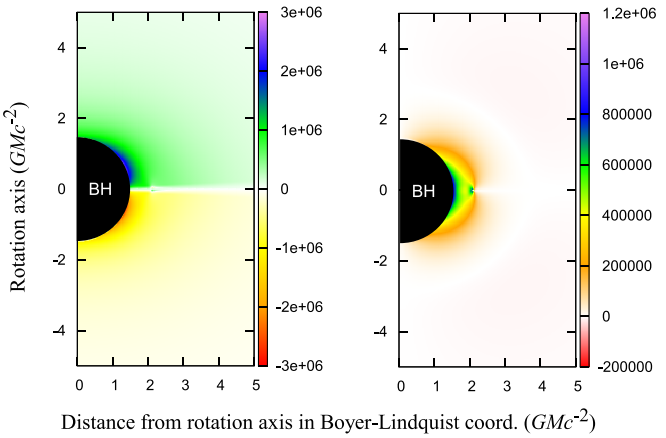

Figure 2. Poloidal magnetic field measured in the ZAMO at $t=0$ for $a=0.9M$. The abscissa and ordinate are the same as Figure 1, but the BH vicinity is closed up. The left and right panels show $B^{\hat{r}}$(ZAMO) and $B^{\hat{\theta}}$(ZAMO), respectively, in Gauss.

except for the equatorial region, where $\tilde{B}^{\hat{r}}$ vanishes by symmetry. To compare with slowly rotating cases, we adopt the same power law in the disk current, $J^\varphi_{\rm eq}\propto r^{-4}$, for all cases of a. To avoid a substantial $|\tilde{B}^{\hat{\theta}}|$ in the lower-latitude ergosphere, we could adopt another functional form of $J^\varphi_{\rm eq}$ for $a\neq 0$; however, such fine-tuning is out of the scope of the present paper.

We assume a positive $J^\varphi_{\rm eq}$; thus, $F_{\theta\varphi}$ (i.e., the radial component of the magnetic field) is positive (or negative) in the northern (or southern) hemisphere. Accordingly, a positive (or negative) sign of $\boldsymbol{E}\cdot\boldsymbol{B}$ indicates that the electric field points outward in the northern (or southern) hemisphere. Thus, as plasmas are created (via photon–photon collisions) near the horizon, $r<2M$, electrons (or positrons) are accelerated inward (or outward) in both hemispheres in this stationary solution. Such accelerated electrons and positrons produce electric currents in the magnetosphere whose poloidal components modify the poloidal electric field through Ampere's law. In the next section, we will focus on the temporal evolution of the electromagnetic fields and the particle distribution functions starting from the initial conditions described in this section.

3. The PIC Scheme

Let us look briefly at the collisionless nature of the plasmas in Section 3.1 before turning to a closer examination of the temporal evolution of the BH magnetosphere in the rest of this section.

3.1. Collisionless Plasmas

Denoting the density of a pair plasma with $n_\pm=\kappa n_{\rm GJ}$, we can express the collision frequency as

$$\nu_{\rm c}\sim\kappa n_{\rm GJ}\sigma c, \tag{26}$$

where σ refers to the collisional cross section, and

$$n_{\rm GJ}\equiv\omega_{\rm H}B/(4\pi ce) \tag{27}$$

denotes the Goldreich–Julian (GJ) number density, which is rotationally induced; e denotes the charge on the electron. If the plasma density is comparable to the GJ value, κ becomes of the order of unity.

Let us evaluate the cross section by $\sigma\sim\pi l_{\rm c}^2$, where $l_{\rm c}$ denotes the typical impact parameter. Equating the potential and kinetic

energies, we find $e^2/l_c \sim (\gamma-1)m_e c^2$. Then, combining it with Equation (26), we obtain

$$\nu_c \sim \frac{\kappa \pi n_{GJ} e^4}{\gamma^2 {m_e}^2 c^3}, \tag{28}$$

where $\gamma \gg 1$ is assumed. On the other hand, the gyrofrequency is given by

$$\nu_B = \frac{eB}{2\pi\gamma m_e c}. \tag{29}$$

We thus obtain

$$\frac{\nu_c}{\nu_B} \sim \frac{\pi}{4}\frac{\kappa}{\gamma}\frac{a}{M}\frac{r_0}{r_H}, \tag{30}$$

where $r_0 \equiv e^2/(m_e c^2)$ denotes the classical electron radius. Since $r_0/r_H \sim 10^{-19} M_1^{-1}$ holds, we can conclude that the collision frequency is much less than the gyrofrequency, and that the assumption of collisionless plasmas in the PIC scheme is justified. This conclusion comes solely from the fact that the GJ density corresponds to a high vacuum in BH or pulsar magnetospheres.

It should be noted that Ohm's law, which is necessary to close the system of equations in MHD, requires that many collisions take place within a single gyration. However, Equation (30) shows that this assumption cannot be justified in a BH magnetosphere unless the plasma density greatly exceeds the GJ value. In the present paper, we thus construct the electric current from the actual motion of charged particles, adopting the PIC scheme. By this method, we can, for instance, incorporate the currents carried by the drift motion of charged particles, as well as the anisotropic distribution of the particles' momenta (e.g., along and perpendicular to the magnetic field lines).

3.2. The Maxwell Equations

In the present paper, we assume $F_{\varphi t} = 0$ throughout the simulations. Accordingly, together with $\partial_\varphi = 0$ for all of the quantities, we find $\partial_t F_{\theta\varphi} = 0$ and $\partial_t F_{\varphi r} = 0$ from Faraday's law. Thus, in the present paper, we treat both B^r and B^θ as constant in time (and hence unchanged from the initial condition) and solve the temporal evolution of only F_{rt}, $F_{\theta t}$, and $F^{r\theta}$. This assumption of $F_{\varphi t} = 0$ is justified as long as the toroidal currents carried by the simulated particles are small compared to the stationary, equatorial toroidal current that is carried by the accreting plasmas.

Under this assumption, Faraday's and Ampere's laws give

$$\frac{\partial F^{r\theta}}{\partial t} = -\frac{\Delta}{\Sigma^2}\left(\frac{\partial F_{\theta t}}{\partial r} - \frac{\partial F_{rt}}{\partial \theta}\right), \tag{31}$$

$$\frac{\partial F_{rt}}{\partial t} = \frac{\Sigma^2}{A}\left[\frac{1}{\sqrt{-g}}\frac{\partial}{\partial\theta}(\sqrt{-g}F^{r\theta}) - 4\pi J^r\right], \tag{32}$$

$$\frac{\partial F_{\theta t}}{\partial t} = \frac{\Sigma^2\Delta}{A}\left[-\frac{1}{\sqrt{-g}}\frac{\partial}{\partial r}(\sqrt{-g}F^{r\theta}) - 4\pi J^\theta\right]. \tag{33}$$

Replacing the r derivatives with r_* derivatives and introducing the following dependent variables,

$$\begin{aligned} B &\equiv \sqrt{-g}F^{r\theta}, \\ D &\equiv F_{rt}, \\ E &\equiv F_{\theta t}\sin\theta, \end{aligned} \tag{34}$$

all of which are well behaved at the horizon, we can rewrite the three Maxwell Equations (31)–(33) into

$$\frac{\partial B}{\partial t} = -c_1\frac{\partial E}{\partial x} + c_2\frac{\partial D}{\partial y}, \tag{35}$$

$$\frac{\partial D}{\partial t} = c_3\frac{\partial B}{\partial y} - 4\pi\frac{\Sigma^2}{A}J^r, \tag{36}$$

$$\frac{\partial E}{\partial t} = -c_4\frac{\partial B}{\partial x} - 4\pi\frac{\Sigma^2}{A}\Delta\sin\theta\cdot J^\theta, \tag{37}$$

where

$$x \equiv r_*, \qquad y \equiv 1-\cos\theta, \tag{38}$$

$$c_1 \equiv \frac{r^2+a^2}{\Sigma}, \qquad c_2 \equiv \frac{\Delta\sin^2\theta}{\Sigma}, \tag{39}$$

$$c_3 \equiv \frac{\Sigma}{A}, \qquad c_4 \equiv \frac{\Sigma(r^2+a^2)}{A}. \tag{40}$$

All of the coefficients, c_1, c_2, c_3, and c_4, are positive definite. Both c_1 and c_4 are close to unity in the entire region. However, $c_2 \ll 1$ holds near the horizon or pole but $c_2 \to 1$ at $r \gg M$ in the lower latitudes. We have $c_3 \ll 1$ at $r \gg M$ and $c_3 \approx 0.25$ near the horizon. Note that the singular behavior (i.e., the polynomial pole) at $\theta = 0$ in Equations (32) and (33) is eliminated by introducing a new meridional coordinate, y.

To solve these three Maxwell equations (Equations (35)–(37)), we must impose appropriate boundary conditions that are consistent with the initial stationary state (Section 2.4). Along the northern and southern polar axes (i.e., at $\theta = 0$ and $\theta = \pi$), we impose

$$B = 0, \quad \frac{\partial D}{\partial y} = 0, \quad E = 0. \tag{41}$$

At the inner boundary, $x = r_* = -\infty$, we impose

$$\begin{aligned} &\frac{\partial B}{\partial x} = 0, \quad \tilde{E}_{\hat{r}} \propto D + \omega F_{r\varphi} = 0, \\ &\frac{\partial E}{\partial x} = \left(\frac{\partial E}{\partial x}\right)_{t=0}, \end{aligned} \tag{42}$$

where the quantity within $()_{t=0}$ indicates the initial value at $t = 0$. At the outer boundary, $x = r_* = r_{out}$, we impose

$$\frac{\partial B}{\partial x} = 0, \quad D = 0, \quad \frac{\partial E}{\partial x} = \left(\frac{\partial E}{\partial x}\right)_{t=0}. \tag{43}$$

Note that we set $B = 0$ in the entire region at $t = 0$.

3.3. Particle Equation of Motion

In a highly vacuum BH magnetosphere, charged leptons are decelerated by the radiation-reaction forces. To include these forces from the first principles, we must adopt tiny time steps and consider the force on one part of the charge by the fields of another part, taking into account retardation within the particle itself. However, in actual simulations, it is unrealistic to adopt

such tiny time steps. Thus, as a compromise, we include the radiation-reaction force as a friction term in the equation of motion (EOM).

With such a friction term, the EOM can be expressed as (Thorne & MacDonald 1982; Hughes et al. 1994; Bacchini et al. 2018)

$$\frac{du_i}{dt} = -\alpha u^t \partial_i \alpha + u_k \partial_i \beta^k - \frac{1}{2}\frac{u_j u_k}{u^t}\partial_i g^{jk} + \frac{q}{m}\left(F_{it} + F_{ij}\frac{u^j}{u^t}\right) + \frac{(F_{\rm rad})_i}{u^t}, \tag{44}$$

where α is defined by Equation (8), $\beta^r = \beta^\theta = 0$, $\beta^\varphi = g_{t\varphi}/g_{\varphi\varphi}$, q/m refers to the charge-to-mass ratio, and

$$u^t = \frac{\sqrt{1 + g^{jk}u_j u_k}}{\alpha}. \tag{45}$$

The Latin indices run over 1, 2, 3. We can evaluate the radiation-reaction force by the covariant form (Section 17.8 of Jackson 1962),

$$F^j_{\rm rad} = \frac{2}{3}\frac{r_0}{c}\left(\frac{d^2u^j}{d\lambda^2} + u^j\frac{du^\nu}{d\lambda}\frac{du_\nu}{d\lambda}\right), \tag{46}$$

where r_0 denotes the classical electron radius, λ denotes the particle's proper time, and the Greek indices run over 0, 1, 2, 3. This radiation-reaction force includes the effects of any kind of acceleration acting on the particles. For instance, photon emissions as a result of the acceleration in an electromagnetic field (e.g., via the synchrocurvature process) and a gravitational field are included (Appendix D). However, this radiation-reaction force does not include the effect of inverse-Compton scattering (ICS), which should be considered separately in future works.

Definition of the four velocity u^μ gives

$$\frac{dr}{dt} = \frac{u^r}{u^t}, \tag{47}$$

$$\frac{d\theta}{dt} = \frac{u^\theta}{u^t}, \tag{48}$$

and

$$\frac{d\varphi}{dt} = \frac{u^\varphi}{u^t}. \tag{49}$$

For presentation purposes, we can convert $u_i = dx_i/d\lambda$ in terms of the ZAMO-measured spatial velocity, $u_{\hat{j}}$, as described in Appendix A.

We integrate Equations (44) and (47)–(49) in the phase space with the global time variable t, which corresponds to the proper time of a distant static observer (i.e., us).

Let us briefly describe the boundary conditions on the motion of electrons and positrons. Due to the symmetry, we assume that the particles moving across the polar axis (at $\theta = 0$ or π) will be reflected equatorward with opposite meridional velocity. Both the inner and outer boundaries are treated as particle sinks. Thus, when particles move across these two radial boundaries, they are excluded from the simulation.

3.4. Plasma Supply

In BH magnetospheres, pairs can be supplied via two- and/or one-photon (i.e., magnetic) pair production processes. In the present paper, we focus on the former process and consider the collisions of MeV photons emitted from the equatorial ADAF via bremsstrahlung. In subsequent papers, we will also consider the collisions between the gap-emitted (inverse-Compton) photons and the ADAF-emitted (synchrotron) photons.

The pair supply rate (pairs per second per volume) is given by

$$\dot{N}_\pm = c\sigma_{\gamma\gamma}{n_\gamma}^2, \tag{50}$$

where $\sigma_{\gamma\gamma}$ denotes the total cross section of photon–photon pair production, and n_γ denotes the MeV photon density. Adopting the Newtonian self-similar ADAF model (Mahadevan 1997) and assuming that the most energetic MeV photons are emitted within $r = 4M$, we obtain (Appendix C)

$$\dot{N}_\pm \approx 1.0 \times 10^{24}\dot{m}^4 {M_1}^{-2}\max\left[\left(\frac{r}{4M}\right)^{-4}, 1\right] \tag{51}$$

in cgs units (i.e., in pairs per second per cubic centimeter).

We randomly introduce a macroparticle in each cell at every time step with probability $1/k_{\rm create} = 0.1$; that is, particles are injected in each cell at every $k_{\rm create} = 10$ time steps, on average. In this case, each created macropositron or -electron has the electric charge

$$q_i = \pm e\dot{N}_\pm k_{\rm create}\Delta_t\Delta_V, \tag{52}$$

where Δ_t denotes the interval of each time step, and Δ_V is the invariant volume of each cell. Note that $\Delta_t\Delta_V = \sqrt{-g}\,dtdrd\theta d\varphi = 2\pi\sqrt{-g}\,\Delta_t\Delta_r\Delta_\theta$ holds, where Δ_r and Δ_θ denote the intervals in Boyer–Lindquist radial and meridional coordinates, both of which are nonuniformly gridded.

In the initial state, there are no macroparticles in any cell. As the PIC simulation proceeds, the number of macroparticles increases with t to saturate at a few hundred in each PIC cell, on average. Here the maximum value of the Courant number is set to be 0.5 for uniform grid intervals in $x = r_*$ and $y = 1 - \cos\theta$ coordinates. In total, there are about 3×10^8 macroparticles in the entire simulation region.

3.5. Nonstationary Magnetosphere

It is checked a posteriori (Section 4.2) that the invariant grid intervals resolve the skin depth,

$$l_{\rm p} = \frac{c}{\omega_{\rm p}}, \tag{53}$$

at every point at any elapsed time, where the plasma frequency $\omega_{\rm p}$ is computed by the plasma density $n_\pm$ and its mean Lorentz factor $\langle\gamma\rangle$ as

$$\omega_{\rm p} = \sqrt{\frac{4\pi e^2 n_\pm}{m_{\rm e}\langle\gamma\rangle}}. \tag{54}$$

For stellar-mass BHs, we obtain

$$\frac{l_{\rm p}}{r_{\rm g}} = 6.84 \times 10^{-2}{k\gamma_6}^{1/2}\left(\frac{a}{M}\cdot\frac{B}{B_{\rm eq}}\right)^{-1/2}{M_1}^{-1/4}, \tag{55}$$

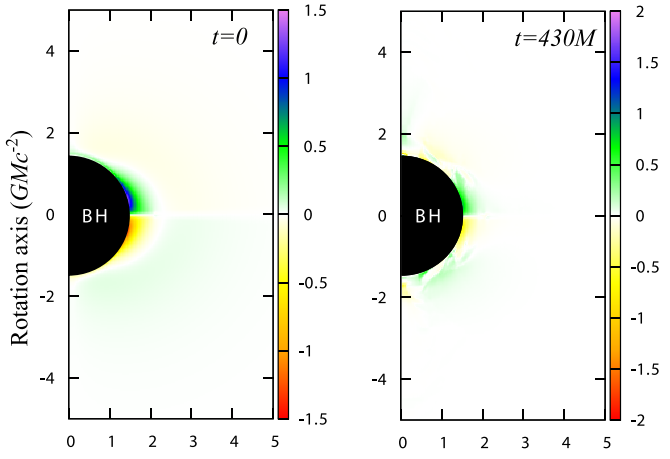

Figure 3. Distribution of $\boldsymbol{E}\cdot\boldsymbol{B}/B_{\rm eq}(2M)^2$ on the poloidal plane $(r,\ \theta)$ for $a=0.9M$, $B=B_{\rm eq}$, and $\dot{m}=2.25\times10^{-4}$. The left and right panels show the distribution at $t=0.00$ and $430.00GMc^{-3}$, respectively. The abscissa and ordinate are the same as Figure 2. Magnetic surfaces (i.e., constant A_φ lines) are not depicted but are the same as the right panel of Figure 1.

where $\gamma_6\equiv\langle\gamma\rangle/10^6$, and

$$k\equiv\kappa^{-1/2}\dot{m}^{-1/4}\left(\frac{r}{r_{\rm H}}\right)^{5/8}\left(\frac{m_{\rm e}}{m_{\rm p}/1836}\right)^{1/2}; \tag{56}$$

$m_{\rm p}$ denotes the rest mass of the proton.

To resolve the skin depth, $l_{\rm p}$, most PIC simulations are performed in one or two dimensions with small ion-to-electron mass ratios (e.g., Bohdan et al. 2019) covering limited time and length scales. In the present paper, adopting a heavy electron mass of $m_{\rm e}=m_{\rm p}/20$, we perform a 2D PIC simulation within about 10 gravitational radii over the time duration of several hundred dynamical timescales. We rescale every expression according to this modified electron mass. Under this assumption of heavy charged leptons, we need about 10^3 grid points to fully resolve the skin depth.

On these grounds, we adopt a radial grid of 960 uniform cells in the range $-15.81807<x<12.82443$, which corresponds to $1.46514M<r<13.68548M$, and 1920 uniform cells in the range $0<y=1-\cos\theta<2$, which corresponds to $0^\circ<\theta<180^\circ$. We present the explicit expression of the discretized Maxwell equations and the particle EOM in Appendix E. To construct the electric currents from particle motion (Appendix F), we adopt the area weighting (Villasenor & Buneman 1992).

3.5.1. Electromagnetic Fields

We start with the magnetic field–aligned electric field. In Figure 3, we present the distribution of $\boldsymbol{E}\cdot\boldsymbol{B}/[B_{\rm eq}(2M)]^2$. For $M=10\,M_\odot$ and $\dot{m}=2.25\times10^{-4}$, we obtain $B_{\rm eq}(2M)=1.452\times10^6$ G. The left and right panels show the distribution of $\boldsymbol{E}\cdot\boldsymbol{B}/[B_{\rm eq}(2M)]^2$ at $t=0$ and $430M$, respectively. In the northern hemisphere, since $F_{\theta\varphi}>0$ holds, a positive (or negative) sign of $\boldsymbol{E}\cdot\boldsymbol{B}$ indicates that an outward (or inward) electric field arises along the local magnetic field lines. In the same manner, in the southern hemisphere, it follows from $F_{\theta\varphi}<0$ that a positive (or negative) sign of $\boldsymbol{E}\cdot\boldsymbol{B}$ means an inward (or outward) electric field.

At $t=0$, there are no poloidal currents in the magnetosphere because of the lack of plasmas. Thus, the magnetic field has no toroidal component. Accordingly, the rotational energy of the BH is not being extracted. On the other hand, because of the relative motion of the magnetic field lines with respect to the spacetime, there appears to be a strong electromagnetic field along the magnetic field line. The left panel of Figure 3 shows that such a magnetic field–aligned electric field is exerted in both hemispheres.

As time elapses, $|\boldsymbol{E}\cdot\boldsymbol{B}|$ evolves, exerting electric currents in the magnetosphere. These currents modify the poloidal electric field through Ampere's law. For example, at $t=430M$ in the northern hemisphere, the right panel shows that a negative $\boldsymbol{E}\cdot\boldsymbol{B}$ appears in the higher–middle latitudes, exerting inward currents there. In the same manner, in the southern hemisphere, $\boldsymbol{E}$ points inward in the higher–middle latitudes outside the ergosphere. Note that $F_{\theta\varphi}$ changes sign across the equator.

Because of this nearly symmetric distribution of the electric field between the two hemispheres, electrons (or positrons) are accelerated outward (or inward) in the higher–middle latitudes in both hemispheres. In the lower latitudes, however, positrons (or electrons) are accelerated outward (or inward) by the strong magnetic field–aligned electric field in both hemispheres. As a result, currents flow inward in the middle latitudes and outward in the lower latitudes. For the details of the electric currents, see Section 3.5.2. Such a pattern of the magnetospheric currents leads to a positive toroidal magnetic field ($\propto F^{r\theta}$) in the northern hemisphere and a negative $F^{r\theta}$ in the southern hemisphere. Thus, $F^{r\theta}$ vanishes on the equator.

Now let us consider the Poynting flux, or, equivalently, the BZ flux,

$$T_{\rm em}{}^r{}_t=\frac{c}{4\pi}F^{r\mu}F_{\mu t}\propto F^{r\theta}F_{\theta t}, \tag{57}$$

in the BH vicinity. If it becomes positive, it means that the BH's rotational energy is being extracted electromagnetically. In Figure 4, we plot the temporal evolution of $T^r_{\rm em}(t,\ r,\ \theta)$ at $r=r_{\rm H}+0.25M$ at four discrete colatitudes as labeled. The ordinate is normalized by the typical BZ flux, which is analytically given by $F_{\rm analytical}\equiv L_{\rm BZ}/S_{\rm area}$, where $S_{\rm area}\equiv\int\int\sqrt{A}\,\sin\theta d\theta d\phi$. The BZ power (i.e., the spin-down luminosity) can be estimated to be

$$L_{\rm BZ}=\frac{1}{128}\left(\frac{a}{M}\right)^2B_\perp{}^2r_{\rm H}{}^2c \tag{58}$$

in the slow-rotating limit, $|a|\ll M$, where $B_\perp$ denotes the average strength of the radial magnetic field. It follows from the figure that the solution exhibits rapid plasma oscillations, as reported by Levinson & Cerutti (2018). It also follows that the simulated BZ flux is consistent with its analytical estimate. See the supplementary material of Crinquand et al. (2020) for a consistent discussion between the simulated BZ flux and their analytical estimates.

It should be noted that the BZ flux increases during the elapsed time $320M<t<450M$ along the middle latitudes, $45^\circ\leqslant\theta\leqslant75^\circ$. During this flux-enhancement phase, the BZ flux (i.e., the Poynting flux) fluctuates relatively mildly compared to its amplitude within $45^\circ\leqslant\theta\leqslant60^\circ$. In the present magnetically dominated magnetosphere, in which the magnetic energy density dominates the particles' rest-mass energy densities, the particles' energy flux is typically less than 10^{-7} compared to the Poynting flux; thus, we neglect their contribution when we consider the energy flux.

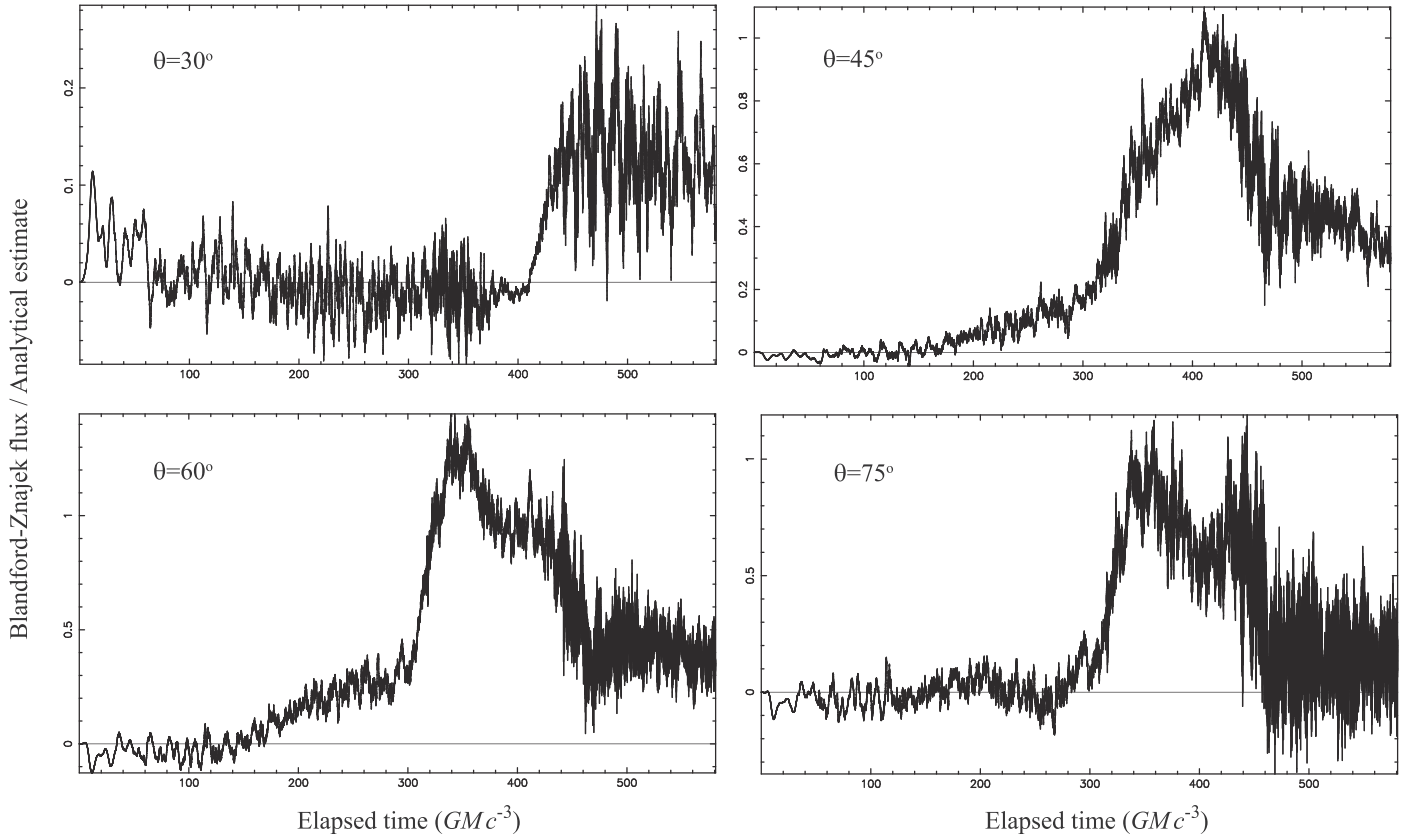

Figure 4. Radial component of the BZ flux as a function of the elapsed time at radius $r = r_{\rm H} + 0.25M$. The ordinate is normalized by its analytical estimate (see text for details), while the abscissa is normalized by the dynamical timescale. Each panel shows the BZ flux at discrete colatitudes as labeled.

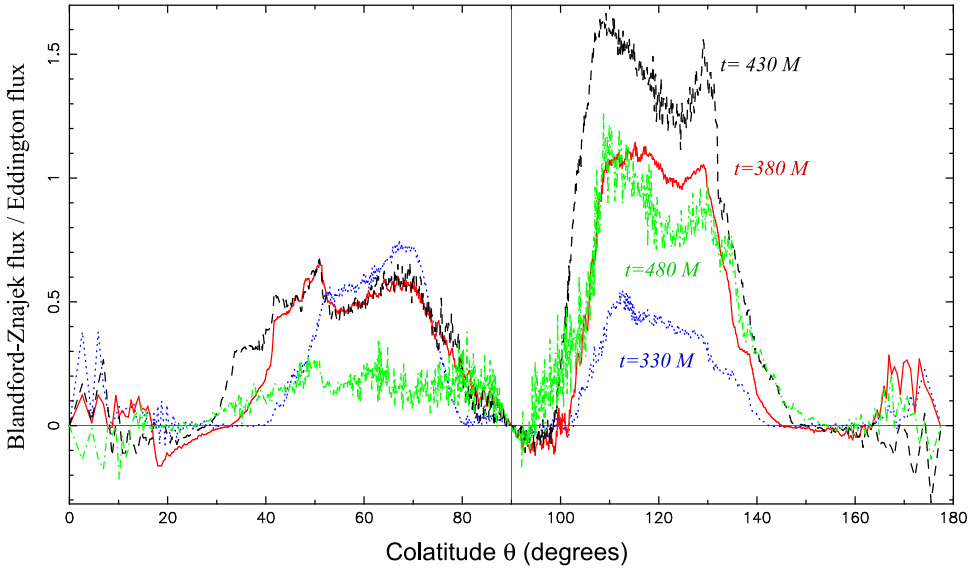

Figure 5. Radial component of the BZ flux as a function of the colatitude angle, θ. The blue dotted, red solid, black dashed, and green dashed–dotted curves show the BZ flux at time $t = 330.00GMc^{-3}$, $380.00GMc^{-3}$, $430.00GMc^{-3}$, and $480.00GMc^{-3}$, respectively.

In Figure 5, we present the angular dependence of the BZ flux at four elapsed times as labeled. During the flux-enhancement phase, the BH's rotational energy is efficiently extracted from the middle latitudes, $40^\circ < \theta < 75^\circ$ in the northern hemisphere and $105^\circ > \theta > 135^\circ$ in the southern hemisphere.

To smear out the variation, we take a moving average with a period of $5GMc^{-3}$ and plot the BZ fluxes in Figure 6. In this particular figure, we compare the results for three accretion rates; the top, middle, and bottom panels show the BZ fluxes at $\dot{m} = 0.000250$, 0.000225, and 0.000200, respectively. We find that the flux is enhanced for typically 140–180 dynamical timescales, and that the flux peaks in the middle latitudes during the enhancement irrespective of the accretion rate, as the blue dashed ($\theta = 50^\circ$), blue solid ($\theta = 60^\circ$), and black dashed ($\theta = 70^\circ$) curves indicate in each panel. For example, at $\theta = 60^\circ$

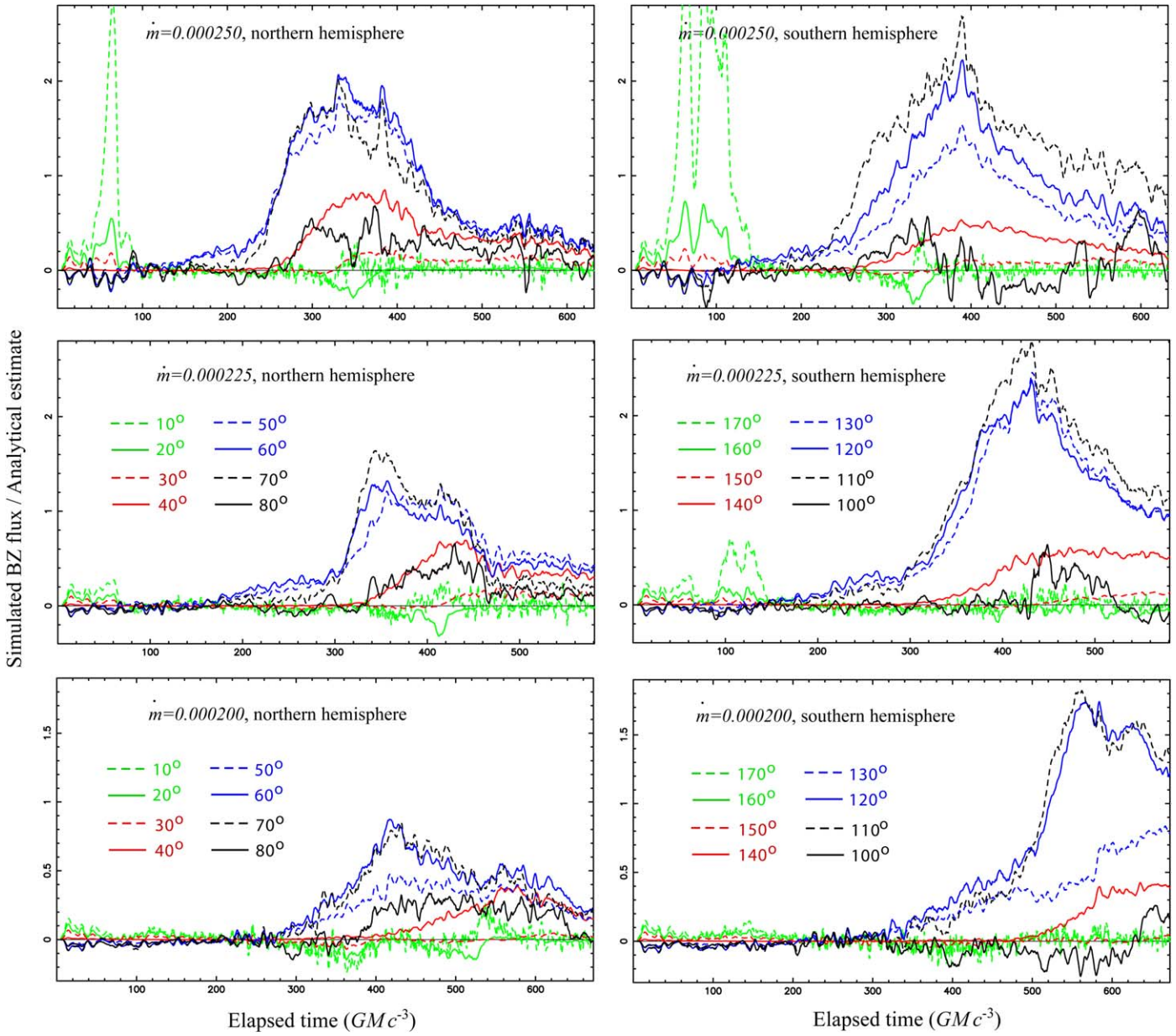

Figure 6. Moving-averaged BZ fluxes with a period of $5GMc^{-3} = 5M$ for three dimensionless accretion rates, $\dot{m} = 2.50 \times 10^{-4}$ (top), $\dot{m} = 2.25 \times 10^{-4}$ (middle), and $\dot{m} = 2.00 \times 10^{-4}$ (bottom). The left (or right) panels depict the BZ flux in the northern (or southern) hemisphere. Each curve denotes the BZ flux at colatitude θ as labeled.

in the northern hemisphere (or $\theta = 120°$ in the southern hemisphere), the FWHMs of the moving-averaged flux become $157M$ and $149M$ in the northern and southern hemispheres, respectively, when $\dot{m} = 2.50 \times 10^{-4}$ (as the top two panels show). They become $136M$ (northern) and $184M$ (southern) when $\dot{m} = 2.25 \times 10^{-4}$ (middle two panels) and $141M$ (northern) when $\dot{m} = 2.00 \times 10^{-4}$ (bottom left panel). However, it is still not possible to measure the FWHM for the southern hemisphere when $\dot{m} = 2.00 \times 10^{-4}$ (bottom right panel). The flux distributes more symmetrically between the northern and southern hemispheres as the accretion rate increases.

3.5.2. Particle Distribution and Currents

We next consider the distribution functions of $e^{\pm}$ and the resultant current distribution. Figure 7 shows the densities of electrons (left) and positrons (middle) at the burst peak, $t = 430M$, in log scale. The right panel shows the GJ value at each point. It follows that both electrons and positrons have greater densities than the GJ value, particularly in the lower latitudes. In the polar regions, because of the polarization drift caused by the varying meridional electric field (and the constant radial magnetic field), electrons migrate meridionally to accumulate in $\theta < 15°$ and $>165°$, whereas positrons are in $15° < \theta < 20°$ and $165° > \theta > 160°$ at $t \sim 430M$. In the lower latitudes, the leptonic densities attain $10^{7.7}$ cm^{-3}.

The charged leptons carry electric currents, as depicted in Figure 8. In the left and right panels, we present the radial and meridional components of the electric currents at each point in the ZAMO frame. For a quantity $f(r, \theta)$, we plot

$$F = \mathrm{sign}\{\lg[\max(|f|, 1)], f\}, \tag{59}$$

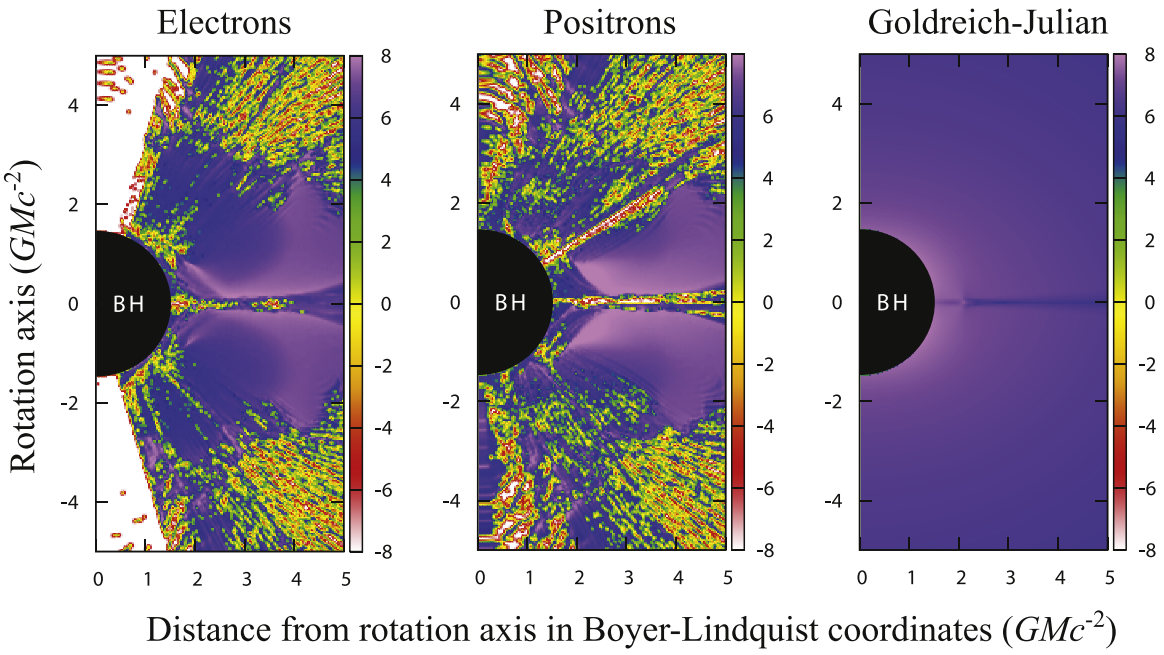

Figure 7. Densities of electrons (left) and positrons (middle) and the GJ density (right), $n_{\rm GJ}$, in cm^{-3} units at $t = 430M$. Values are plotted in decadic logarithm. The abscissa and ordinate are the same as Figure 2.

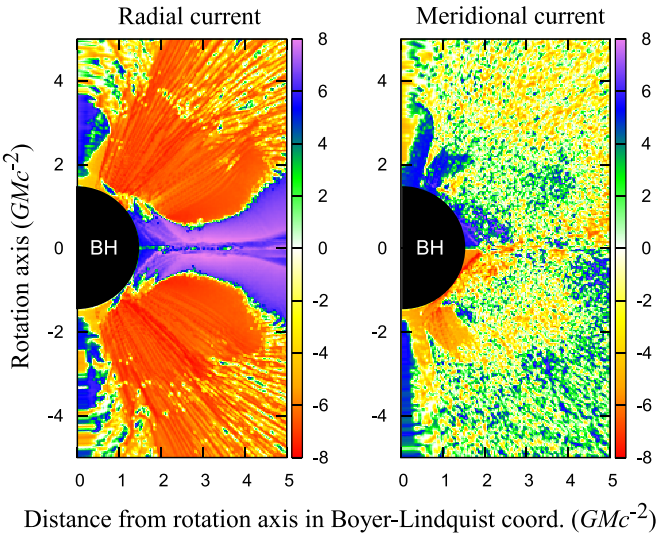

Figure 8. Electric currents measured by the ZAMO in the poloidal plane at $t = 430M$. The abscissa and ordinate are the same as Figure 2. The left panel shows the radial component, $J^{\hat{r}}$, while the right panel shows the meridional component, $J^{\hat{\theta}}$. To plot the values, we take the decadic logarithm of the absolute value of a quantity, then put the same sign as the quantity. For example, in the left panel, the value of 10^6 (or -10^6) corresponds to an outward (or inward) current density whose absolute value is 10^6 statampere cm^{-2}. In the same way, in the right panel, a positive (or negative) $J^{\hat{\theta}}$ means an equatorward current in the northern (or southern) hemisphere.

where sign$(a,\ b) = |a|$ if $b \geqslant 0$ and $= -|a|$ if $b < 0$; we set $f = J^{\hat{r}}$ and $J^{\hat{\theta}}$ for the left and right panels, respectively. In the left panel, the yellow–red regions show that currents flow inward in the middle latitudes, while the blue–violet regions show that they flow outward in the lower latitudes. These radial currents are closed by meridional currents flowing within the ergosphere, as the right panel shows. For example, in the right panel, the blue (or red) region in the lower–middle latitudes within $r < 2M$ in the northern (or southern) hemisphere shows equatorward meridional currents. Because of this current closure, it is confirmed that the BZ process is, indeed, facilitated.

To grasp the current distribution more easily, we plot the direction and strength of the poloidal currents as red arrows in Figure 9. The current density is averaged over the area in which we compute the direction and length of each arrow. In the figure, the length of the arrows indicates the strength of the current density in logarithmic scale, as indicated by the right panel. We can confirm the current pattern discussed in the foregoing paragraph. It also follows that the averaged currents mostly flow in the middle and lower latitudes; thus, the low-density regions in the polar funnels do not essentially affect the entire structure of the magnetosphere. In this figure, we also plot the charge density, $(n_+ - n_-)/n_{\rm GJ}$, in color, where n_+ and n_- refer to the positronic and electronic number densities. Values are plotted using the same method as Figure 8 (Equation (59)). It follows that the real charge density becomes even greater than the GJ value (right panel of Figure 7), which indicates that the electron–positron plasmas become highly nonneutral near the BH.

We next consider the distribution functions of the charged leptons. The dimensionless distribution functions of $e^{\pm}$, $n_{\pm}$, are sliced between the colatitude $\theta_1 < \theta < \theta_2$,

$$N_{\pm}(r_*,\ \gamma) \equiv \frac{1}{n_{\rm GJ}} \int_{\theta_1}^{\theta_2} d\theta \frac{\partial^2 n_{\pm}(r_*,\ \theta,\ \gamma)}{\partial\theta\partial\gamma}. \tag{60}$$

In Figure 10, we present N_- and N_+ as a function of r_* and γ (i.e., the Lorentz factor) in the left and right columns, respectively. The range of $\theta \in [\theta_1,\ \theta_2)$ increases from the top to bottom rows as described in the caption. It shows that the Lorentz factors are saturated at a terminal value at each point. The terminal value is determined by the balance between the electrostatic acceleration and the synchrocurvature radiation drag force. Since $|\boldsymbol{E}\cdot\boldsymbol{B}|$ significantly increases with decreasing radius at $r_* < 0$ (or, equivalently, $r < 4.1M$), particles gain

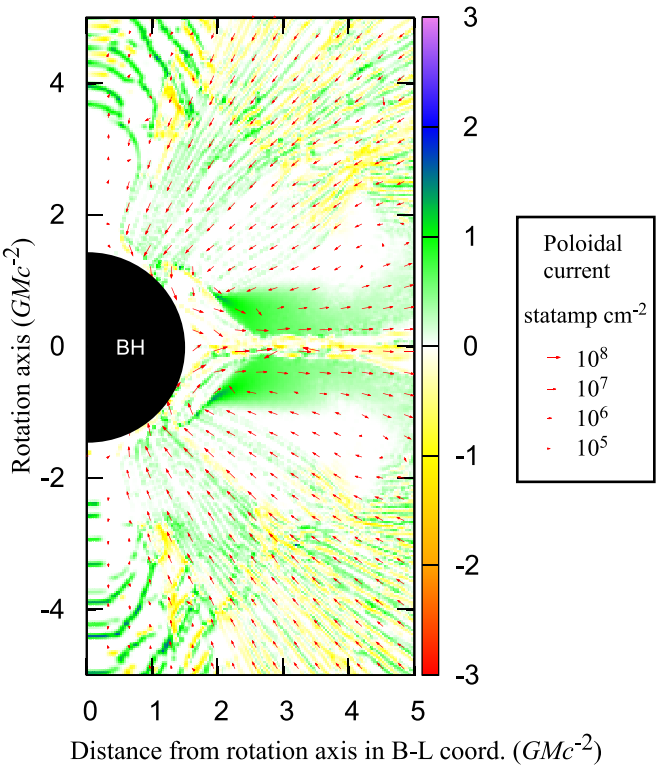

Figure 9. Dimensionless charge density $(n_+ - n_-)/n_{\rm GJ}$ (color image) and poloidal electric current (red arrows). The abscissa and ordinate are the same as Figure 2. The charge density is plotted in linear scale. The green (or yellow) regions show positive (or negative) dimensionless charge densities. The right panel shows four example arrow lengths corresponding to the indicated strengths of the poloidal current densities in statampere cm^{-2}.

large kinetic energies inside $r < 4M$. Nevertheless, by virtue of the residual magnetic field–aligned electric field, particle motion is kept relativistic in the entire region. Lorentz factors attain $\gamma > 10^{4.5}$ in $r_* < 1M$ (or, equivalently, $r < 4.7M$).

To examine the pitch-angle dependence, in Figure 11, we plot $N_\pm(r_*, \chi)$, where the pitch angle χ becomes $+1$ (or -1) when a particle is moving outward (or inward) with a very small trans-magnetic-field momentum and becomes zero when it has no longitudinal momentum. At $r_* > 0$, particles have small trans-magnetic-field momenta. However, in the higher–middle latitudes, $\theta \sim 40°$, the middle panels show that electrons (or positrons) migrate outward with positive $\cos\chi$ (or inward with negative $\cos\chi$), indicating an inward poloidal current there. Figures 10 and 11 show that particles are highly relativistic with nonthermal and anisotropic distribution functions.

4. Discussion

To sum up, we simulated the evolution of a BH magnetosphere by a PIC scheme, when a poloidal magnetic field is sustained by a disk toroidal current and the electron–positron pair plasmas are steadily supplied homogeneously per invariant volume basis. Provided that the mass accretion rate is much less than the Eddington rate, both the electromagnetic fields and the particle distribution functions exhibit rapid variability. The rotational energy of the BH is, indeed, extracted via the BZ process, whose energy flux concentrates in the middle latitudes, particularly during the flux-enhancement phase that lasts approximately 160 ± 20 dynamical timescales. We have demonstrated that the collision timescale is much longer than the gyration timescale (i.e., the Ohm's law cannot be justified), the pair plasma is highly nonneutral, the particles' energy distribution is non-Maxwellian, and the momentum distribution is anisotropic. Thus, we must discard the MHD approximation when we consider the jet-launching region around the BH whose mass accretion rate is highly sub-Eddington.

In this section, we discuss the dominant radiative process in Section 4.1, the validity of gridding in Section 4.2, a comparison with other works in Section 4.3, and an implication for the collimation of VLBI jets in Section 4.4.

4.1. Dominant Radiative Process

Although the synchrocurvature radiation process is incorporated in the radiative reaction force, $F^j_{\rm rad}$, ICS is not considered as a radiation drag. Thus, we have to confirm that the ICS process is negligible compared with the synchrocurvature process around stellar-mass BHs accreting at $\dot{m} \ll 1$. Here we briefly compare the pure curvature, pure synchrotron, and ICS processes and discuss the dominant process. To make a general discussion, we adopt the actual electron mass $m_{\rm e} = m_{\rm p}/1836$, instead of $m_{\rm p}/20$, in this subsection.

The magnitude of the radiation drag force due to the pure curvature process is given by

$$F_{\rm curv} = \frac{2}{3} e^2 \frac{\gamma^4}{\rho_{\rm c}^2} = 1.70 \times 10^{-4} \left(\frac{\rho_{\rm c}}{2M}\right)^{-2} M_1{}^{-2} \gamma_7{}^4 \,{\rm dyn}, \quad (61)$$

where $\rho_{\rm c}$ refers to the curvature radius of the particle's center of gyration, $2M = 2MGc^{-2}$ is the Schwarzschild radius, and $\gamma_n \equiv \gamma/10^n$. If this force balances with the electrostatic force,

$$eE_\parallel = 4.80 \times 10^{-5} |E_{\parallel,5}| {\rm dyn}, \quad (62)$$

we find that the particles saturate at the Lorentz factor,

$$\gamma_{\rm curv} = 7.28 \times 10^6 \left(\frac{\rho_{\rm c}}{2M}\right)^{1/2} M_1{}^{1/2} E_{\parallel,5}{}^{1/4}, \quad (63)$$

where $E_{\parallel,5} \equiv E_\parallel/(10^5\,{\rm statvolt\ cm^{-1}})$.

The magnitude of the radiation drag force due to the pure synchrotron process is given by

$$F_{\rm sync} = \frac{2}{3} r_0{}^2 \gamma^2 B^2 \sin^2\chi = 5.29 \times 10^{-5} \gamma_5{}^2 B_6{}^2 \frac{\sin^2\chi}{0.1} \,{\rm dyn}, \quad (64)$$

where r_0 denotes the classical electron radius, and χ is the pitch angle. Equating Equations (62) and (64), we obtain the terminal Lorentz factor,

$$\gamma_{\rm sync} = 9.52 \times 10^4 B_6{}^{-1} \left(\frac{\sin^2\chi}{0.1}\right)^{-1/2} E_{\parallel,5}^{1/2}. \quad (65)$$

If $\gamma_{\rm sync} < \gamma_{\rm curv}$, the pure synchrotron process dominates the pure curvature process. If $m_{\rm e} = m_{\rm p}/1836$, we find that the condition $\gamma_{\rm sync} < \gamma_{\rm curv}$ is satisfied because

$$B_6 \left(\frac{\sin\chi}{0.1}\right) E_{\parallel,5}^{-1/4} \left(\frac{\rho_{\rm c}}{2M}\right)^{1/2} > 1 \quad (66)$$

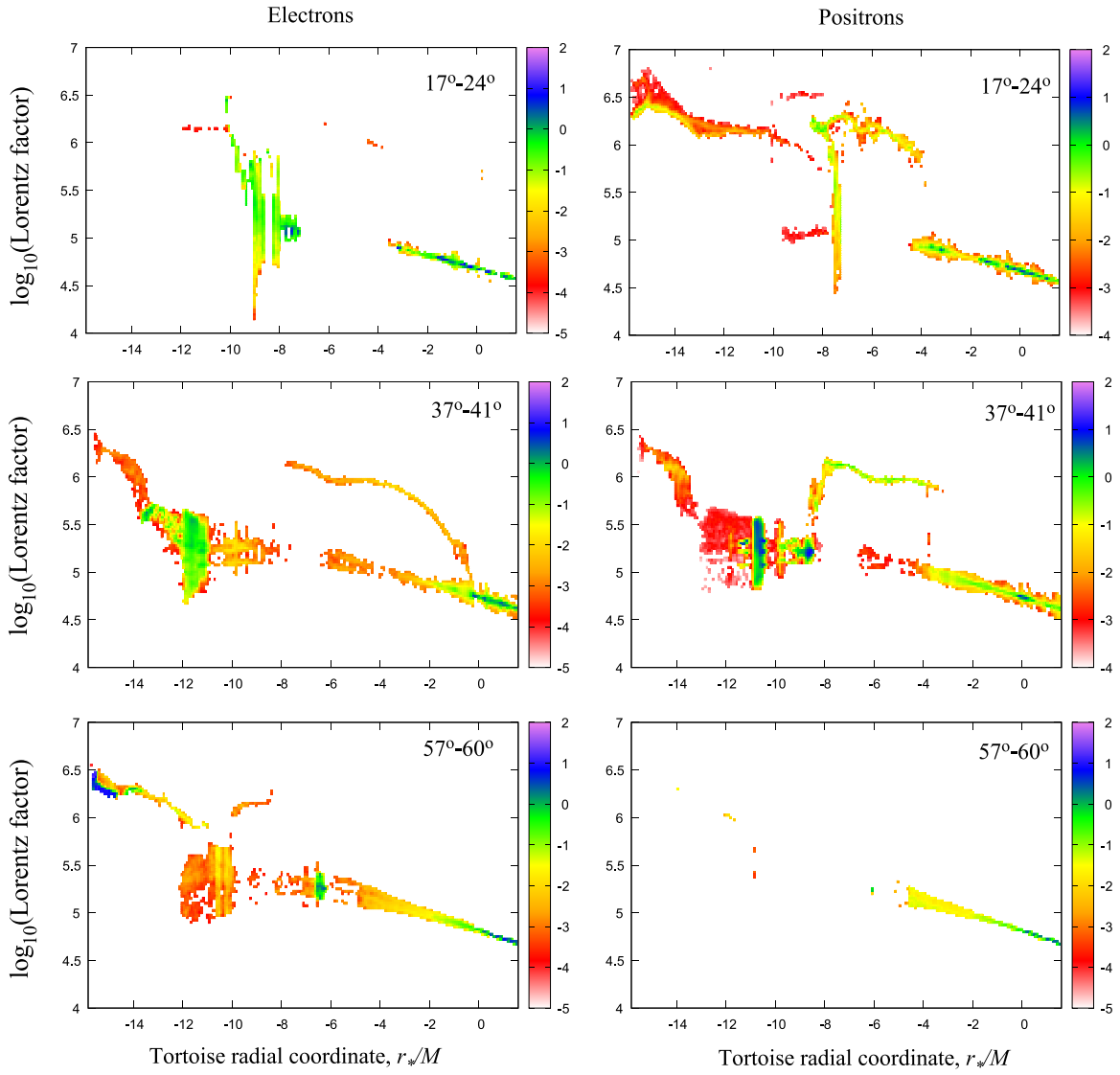

Figure 10. Lorentz factor dependence of the distribution of electrons (left) and positrons (right) as a function of the dimensionless tortoise coordinate, r_*/M, at elapsed time $t = 430M$. The colors show the logarithmic value of the dimensionless distribution functions (see text) along discrete colatitudes. The top, middle, and bottom rows show the distribution function in the meridional range 16.°606–23.°568, 37.°678–41.°432, and 57.°235–60.°034, respectively.

is satisfied by the vast majority of the particles. Put another way, the synchrocurvature process reduces to the pure synchrotron process for most of the particles. However, since we assume heavy electrons in this paper, the increased gyroradius makes the synchrotron process less efficient; thus, the radiation drag force is given by the synchrocurvature process in general for heavy electrons.

We next compare the pure synchrotron process with the ICS. At a radius r from the central BH, the number density of the ADAF synchrotron photons is given by Mahadevan (1997),

$$N_{\rm ph} = \frac{L_{\rm sync}}{4\pi r^2 h\nu c}, \tag{67}$$

where $h\nu$ refers to the energy of the photons emitted from the ADAF via the synchrotron process. The synchrotron luminosity is given by

$$L_{\rm sync} = 1.67 \times 10^{36} {M_1}^{1/2} \dot{m}^{3/2} \ {\rm erg\ s^{-1}}. \tag{68}$$

The typical photon energy is given by Equation (22) of Mahadevan (1997). Accordingly, we obtain

$$N_{\rm ph} = 1.55 \times 10^{20} {T_{\rm e,9}}^5 M_1 \dot{m} \ {\rm photons\ cm^{-3}}, \tag{69}$$

where $T_{\rm e,9}$ refers to the electron temperature, $T_{\rm e}$, normalized by 10^9 K. The ICS drag force per electron (or positron) is given by

$$F_{\rm ICS} \approx N_{\rm ph} \sigma_{\rm KN} \gamma m_{\rm e} c^2, \tag{70}$$

where

$$\sigma_{\rm KN} \approx \frac{3}{8}\sigma_{\rm T} x^{-1}\left(\ln 2x + \frac{1}{2}\right) \tag{71}$$

refers to the Klein–Nishina cross section, and $x \approx \gamma$ holds on average. We thus have

$$F_{\rm ICS} \approx 3.89 \times 10^{-10} M_1 \dot{m} {T_{\rm e,9}}^5. \tag{72}$$

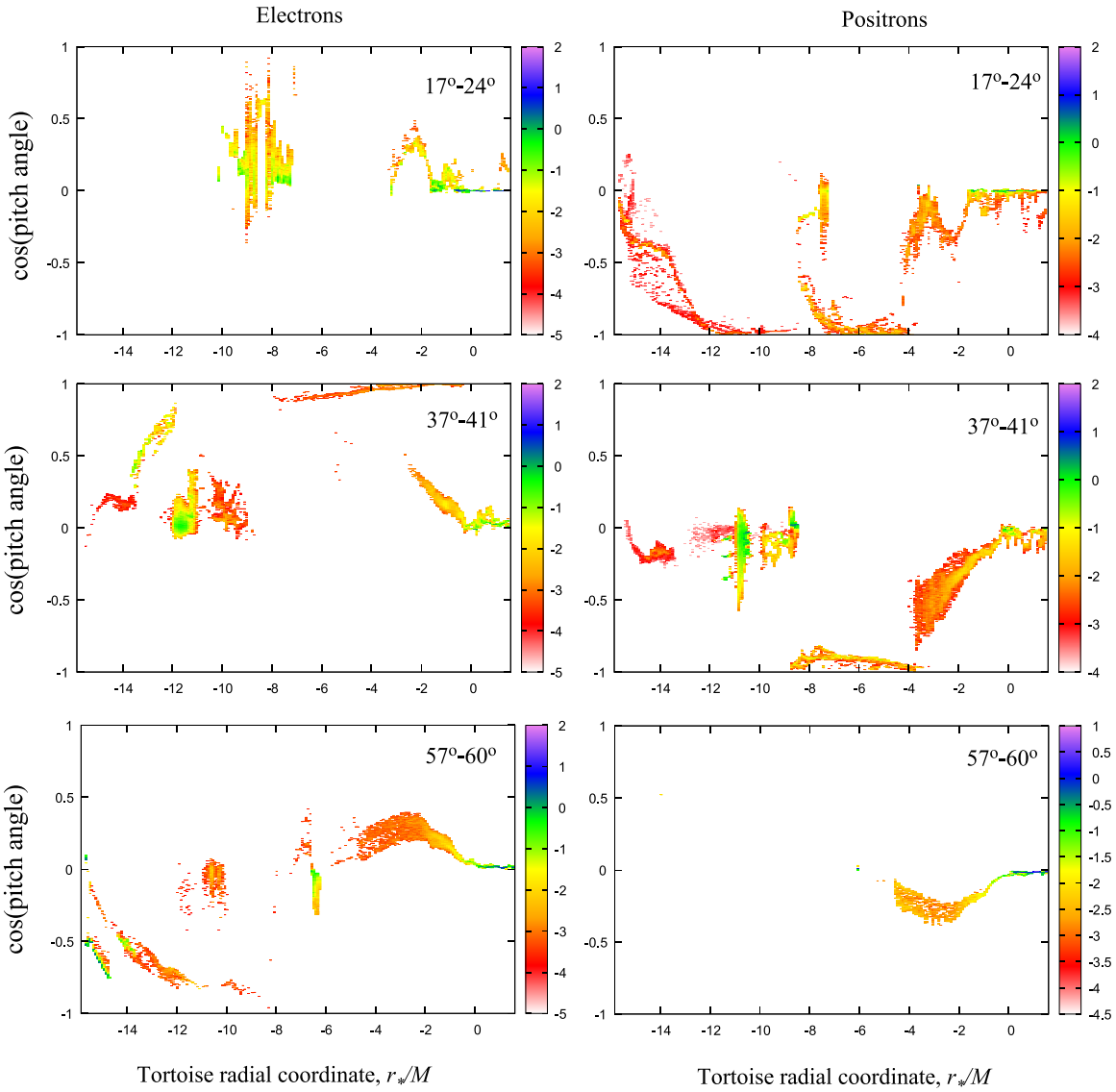

Figure 11. Similar to Figure 10 but showing the pitch-angle dependence of the distribution functions of electrons (left) and positrons (right) at $t = 430M$. The colors show the logarithmic value of the dimensionless distribution functions within the same meridional range as Figure 10.

We thus obtain

$$\gamma_5{}^2 B_6{}^2 \left(\frac{\sin\chi}{0.1}\right)^2 M_1^{-1}\dot{m}^{-1}T_{e,9}{}^{-5} \gg 10^{-5}. \quad (73)$$

On these grounds, we obtain $F_{\rm sync} \gg F_{\rm curv} \gg F_{\rm ICS}$ for the actual electron mass. Note that the Lorentz factor will increase with decreasing electron mass. However, for heavy electrons, energy transfer efficiency increases due to their greater mass ratio to protons. Thus, ICS may not be negligible even for stellar-mass BHs. However, we neglected ICS in this paper, considering a future extension to smaller electron masses.

In short, for the actual electron mass, it is possible that the ICS process is negligible compared to the synchrocurvature process when we consider stellar-mass BHs in a quiescent state. However, for supermassive BHs, we generally obtain $F_{\rm ICS} > F_{\rm curv} \gg F_{\rm sync}$ because of the large curvature radius and weak magnetic field strength (Hirotani et al. 2016) for the actual electron mass.

Table 1
Invariant Grid Interval, $\epsilon(r, \theta) = \Delta_s/r_{\rm g}$

$r/r_{\rm g}$	$\theta = 2.^\circ62$	$29.^\circ0$	$60.^\circ0$	$90.^\circ0$
8.507	0.2762	0.0262	0.0261	0.0260
4.099	0.1355	0.0217	0.0215	0.0214
2.021	0.0714	0.0122	0.0117	0.0114
1.471	0.0557	0.0036	0.0028	0.0026

4.2. Grid Interval versus Skin Depth

Let us compare the invariant grid interval $\epsilon\, r_{\rm g} \equiv \Delta_s \equiv \max\left(\sqrt{g_{rr}}\Delta_r, \sqrt{g_{\theta\theta}}\Delta_\theta\right)$ with the skin depth, $l_{\rm p}$ (Equation (53)), where Δ_r and Δ_θ denote the interval in r and θ coordinates, respectively. Representative values of the dimensionless function $\epsilon(r, \theta)$ are presented in Table 1. Because of a constant $\sin\theta\Delta_\theta$ gridding, Δ_θ increases with decreasing $\sin\theta$. Note that the dimensionless grid interval ϵ is defined independently from the BH mass.

Adopting heavy electrons, $m_e = m_p/20$, and normalizing the skin depth with r_g, we obtain

$$\frac{l_p}{r_g} = 3.4(\gamma_5 n_5^{-1})^{1/2}, \quad (74)$$

where $\gamma_\nu \equiv \langle\gamma\rangle/10^\nu$ and $n_\nu \equiv n_\pm/10^\nu$; $\langle\gamma\rangle$ denotes the average Lorentz factor. The highest-density region appears in the lower latitudes at $r < 4M$, i.e., at $r_* < -0.25M$. In this region, $n < 10^{7.7}\,\mathrm{cm}^{-3}$ and $\langle\gamma\rangle > 10^{4.7}$; thus, we obtain $l_p > 0.108 r_g > 5\Delta_s$ there. Other regions have greater skin depth. Accordingly, the skin depth can be resolved at every point (and, in fact, at every time step) during the PIC simulation, although it is marginal when $l_p \sim 5\Delta_s$ happens at the flux peak.

4.3. Comparison with Previous Works

Let us compare the present work with two recent works on 2D GR PIC simulations (Parfrey et al. 2019; Crinquand et al. 2020).

First, we discuss the difference with Parfrey et al. (2019). Ignoring radiative transfer and instead considering an injection of pairs whose rate is proportional to the local magnetic field–aligned electric field, they performed 2D GR PIC simulations of the magnetosphere of an extremely rotating BH with $a = 0.999M$. The BH mass is not explicitly specified in their paper but is presumably supermassive. They adopted an extremely small magnetic field strength to emphasize the Penrose process, an energy-extraction mechanism from rotating BHs when particles fall onto the horizon with negative energies measured at infinity. Particles were created in the reconnecting current sheet on the equatorial plane. The magnetization parameter was 2000; that is, the magnetosphere was still magnetically dominated. Magnetic field configuration is initially Wald's vacuum solution, which is produced by a toroidal ring current flowing on the equatorial plane at large distances. Then the field lines are bent back toward the BH to penetrate the horizon. For M87*, their dimensionless magnetic field strength, $\tilde{B}_0 = 10^3$, corresponds to the actual strength, $B = \tilde{B}_0(m_e c^2/e r_g) \sim 10^{-9}$ G, which is about 10^{-11} times smaller than what is observed (Event Horizon Telescope Collaboration et al. 2019). Under this condition, they found that the charged leptons created in the current sheet plunge onto the horizon with negative energies as a result of the interaction with the electromagnetic field, and that the Penrose process contributes to the extraction of the energy and angular momentum from a maximally rotating BH.

In the present paper, on the other hand, we consider a stellar-mass BH. In this case, we can resolve the skin depth with a realistic magnetic field strength, $B = B_{eq}$. Accordingly, the magnetization parameter becomes of the order of 10^7; thus, we did not mention the particle contribution on the energy extraction from a rotating BH. Nevertheless, the particle energy flux does become negative in our simulation as well; thus, the Penrose process is indeed working, although their contribution is negligible. We assume a homogeneous and constant plasma supply in the present work, which forms a contrast to Parfrey et al. (2019), who considered pair creation in the reconnecting current sheet. The magnetic field is assumed to be fixed on the poloidal plane during the simulation in the present paper.

Second, let us discuss the difference with Crinquand et al. (2020). In their 2D GR PIC code, implementing ICS and photon–photon pair production self-consistently, they solved the PIC equations together with the radiative transfer equation. Electron–positron pair plasmas are supplied in response to gap opening. They presumed supermassive BHs. In this case, ICS dominates the pure curvature radiation (Hirotani et al. 2016), where the particle's pitch angles become small enough due to the ICS and continuous acceleration along the magnetic field lines (Beskin et al. 1992). Thus, their treatment, which takes account of only the ICS as radiative processes, can be justified. Crinquand et al. (2020) assumed a true monopole magnetic field whose radial component points outward in the entire magnetosphere. Accordingly, no current sheets appear in their solution. Electric currents flow inward (or outward) in the northern (or southern) hemisphere, leading to a negative $F^{r\theta}$ in the entire magnetosphere. Since $E_\theta = F_{\theta t} > 0$ holds in both hemispheres, the resultant Poynting flux is also positive in both hemispheres. In their Zelton code, they solved all six components of the electromagnetic fields, computing the evolution of $F_{\varphi t}$ from the toroidal component of the current density J^φ that is constructed from the azimuthal motion of the charged particles.

In the present paper, on the other hand, instead of solving the radiative transfer equation, we simply adopt a uniform and constant pair production in the particle source term. We consider a stellar-mass BH, in which case the synchrocurvature process becomes nonnegligible compared to ICS (Hirotani et al. 2016). We assume a split-monopole magnetic field whose radial component is positive (or negative) in the northern (or southern) hemisphere. Accordingly, a current sheet appears on the equator. Electric currents flow inward in the higher latitudes in both hemispheres and outward in the lower latitudes, leading to a negative (or positive) $F^{r\theta}$ in the northern (or southern) hemisphere and a positive BZ flux in both hemispheres, as discussed in Section 3.5.1.

Let us briefly point out the limitation of the present analysis. Unlike the Zelton code, we solved only three of the six components of the electromagnetic fields in the present paper, putting $F_{\varphi t} = 0$, and hence $\partial_t F_{\theta\varphi} = \partial_t F_{\varphi r} = 0$ throughout the simulation, as the first step. If the local physics (as supposed in recent 1D GR PIC simulations) does not significantly affect the entire structure of the magnetosphere, such an assumption of a fixed poloidal magnetic field could be justified. However, when we apply the present 2D method to a global magnetosphere, toroidal currents carried by the charged leptons at each position can alter the entire magnetic field configuration on the poloidal plane. Thus, in the same manner as in recent 1D models (Levinson & Cerutti 2018; Chen & Yuan 2020; Kisaka et al. 2020), we must draw attention to the limitation of $F_{\varphi t} = 0$. In the next paper, we will extend our analysis to the case $F_{\varphi t} \neq 0$, constructing J^φ at each position from the actual motion of the charged leptons and solving all six components of the electromagnetic fields.

4.4. Implication for Supermassive BHs

Let us finally discuss what can be expected if the present results obtained for stellar-mass BHs can be applied to supermassive BHs. We have demonstrated that the BH's rotational energy is efficiently extracted along the magnetic field lines that cross the event horizon in the middle latitudes. Let us discuss an implication of this result on the formation of limb-brightened jets. It has been revealed by the VLBA observations in 15–43 GHz that the innermost region of the M87 jet exhibits a limb-brightened structure (Junor et al. 1999;

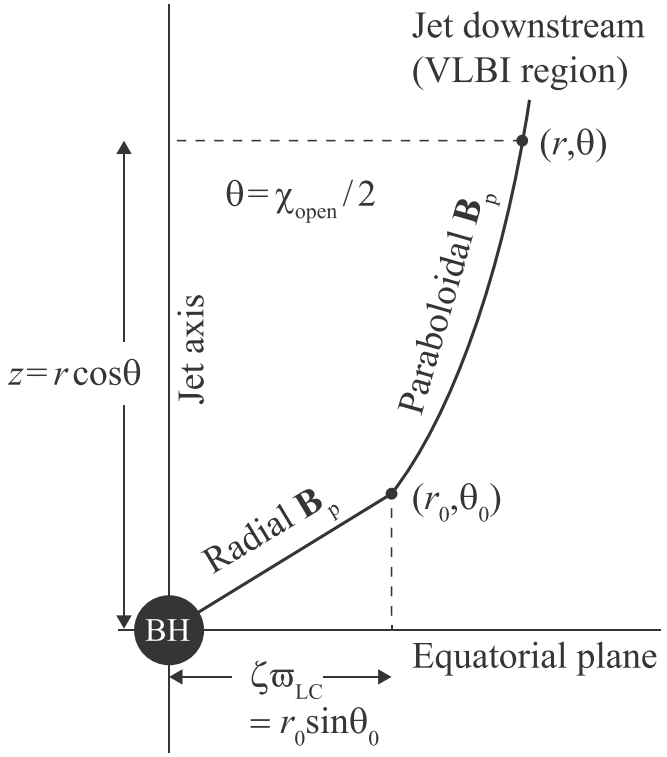

Figure 12. Schematic picture of the jet downstream region. The jet shape is assumed to be radial inside the radius r_0 and paraboloidal outside of it. The jet is observed with VLBI at radius r. Both θ and θ_0 are measured from the jet axis, which coincides with the BH's rotation axis.

Kovalev et al. 2007; Ly et al. 2007; Hada et al. 2011, 2013; Walker et al. 2018). At 86 GHz, this limb-brightened structure is already well developed at 0.15 mas from the VLBI core, where the corresponding apparent opening angle becomes approximately 100° (Hada et al. 2016). If a relatively large viewing angle of $\theta_{\rm view}\sim 30^\circ$ is adopted (Ly et al. 2007; Hada et al. 2016), the jet has a deprojected opening angle $\chi_{\rm open}\sim 50^\circ$ at the deprojected distance $z = 84GMc^{-2}$. However, if a smaller viewing angle, $\theta_{\rm view}\sim 17^\circ$, is adopted (Biretta et al. 1999; Wang & Zhou 2009; Perlman et al. 2011; Nakamura & Meier 2014; Mertens et al. 2016; Walker et al. 2018), we obtain $\chi_{\rm open}\sim 30^\circ$ at $z = 108GMc^{-2}$.

If a jet begins to collimate outside the outer light surface (Camenzind 1986), we may assume that the jet is radial within the distance $\zeta\,\varpi_{\rm LC}$ from the rotation axis and becomes paraboloidal outside of it (Asada & Nakamura 2012; Hada et al. 2013; Nakamura & Asada 2013; Asada et al. 2016; Nakamura et al. 2018), where $\varpi_{\rm LC}\equiv c/\Omega_{\rm F}$ denotes the typical radius of the outer light surface. Figure 12 sketches the geometry of this jet downstream region. Assuming that we observe the jet at the position (r, θ), we can express ζ in terms of the observables z and $\theta=\chi_{\rm open}/2$ as $r(1-\cos\theta)=(\zeta\varpi_{\rm LC}/\sin\theta_0)(1-\cos\theta_0)$, which gives

$$\zeta\approx\frac{z}{\varpi_{\rm LC}}\frac{1-\cos\theta}{\cos\theta}\frac{\sin\theta_0}{1-\cos\theta_0}, \tag{75}$$

where $z=r\cos\theta$. If $\Omega_{\rm F}\approx 0.5\omega_{\rm H}$, $a\approx 0.9M$ gives $\varpi_{\rm LC}\approx 6.4GM/c^2$. (Note that $\Omega_{\rm F}=F_{t\theta}/F_{\theta\varphi}$ is not assumed but solved in the PIC simulation.) If the magnetic field line with the footpoint angle $\theta_0\approx 60^\circ$ (or 75°) is brightened at downstream z with a half opening angle $\theta=\chi_{\rm open}/2$, we obtain $\zeta\approx 2.4$ (or $\zeta\approx 1.8$) for $\theta_{\rm view}=30^\circ$ and $\zeta\approx 1.0$ (or $\zeta\approx 0.78$) for $\theta_{\rm view}=17^\circ$ using the 86 GHz VLBI observations. On these grounds, if the BZ flux concentrates in the middle latitudes also in the case of supermassive BHs, it is possible that the M87 jet begins to collimate slightly outside the outer light surface, typically within a distance of $2.4\varpi_{\rm LC}$ from the rotation axis, which may become a good target of the Event Horizon Telescope and GRAVITY.

We thank the anonymous referee for careful reading and valuable comments on this manuscript. The authors acknowledge grant support to the CompAS/Antares group, and the access to the high-performance computing facility from the Institute of Astronomy and Astrophysics in Academia Sinica (ASIAA). The authors acknowledge grant support from Ministry of Science and Technology (MoST) under grant Nos. 105-2119-M-001-044-MY3, 108-2112-M-001-009- and 109-2112-M-001-028-.

Appendix A
ZAMO-measured Quantities

We give the expressions of ZAMO-measured quantities, which are indicated by a tilde (~), in this appendix. Using Equations (4)–(7), we obtain

$$u_{\hat r}=\sqrt{\frac{\Delta}{\Sigma}}\,u_r, \tag{A1}$$

$$u_{\hat\theta}=\sqrt{\frac{1}{\Sigma}}\,u_\theta, \tag{A2}$$

$$u_{\hat\varphi}=\sqrt{\frac{A}{\Sigma}}\,\sin\theta u_\varphi; \tag{A3}$$

or, equivalently, their contravariant components become

$$u_{\hat r}=u^{\hat r}\equiv\sqrt{g_{rr}}u^r, \tag{A4}$$

$$u_{\hat\theta}=u^{\hat\theta}\equiv\sqrt{g_{\theta\theta}}u^\theta, \tag{A5}$$

$$u_{\hat\varphi}=u^{\hat\varphi}\equiv\sqrt{g_{\varphi\varphi}}(u^\varphi-\omega u^t), \tag{A6}$$

$$u^j\equiv\gamma v^j, \tag{A7}$$

where

$$\gamma\equiv\frac{1}{\sqrt{1-\boldsymbol{v}\cdot\boldsymbol{v}}}. \tag{A8}$$

In the same way, the tetrad transformation law gives the following expressions of the electromagnetic fields in the ZAMO:

$$\tilde E_{\hat r}=\boldsymbol{F}(\tilde{\boldsymbol{e}}_{(\hat r)},\tilde{\boldsymbol{e}}_{(\hat t)})=\frac{\sqrt{(r^2+a^2)^2-\Delta a^2\sin^2\theta}}{\Sigma}(F_{rt}+\omega F_{r\varphi}), \tag{A9}$$

$$\tilde E_{\hat\theta}=\boldsymbol{F}(\tilde{\boldsymbol{e}}_{(\hat\theta)},\tilde{\boldsymbol{e}}_{(\hat t)})=\frac{\sqrt{(r^2+a^2)^2-\Delta a^2\sin^2\theta}}{\sqrt{\Delta}\,\Sigma}(F_{\theta t}+\omega F_{\theta\varphi}), \tag{A10}$$

$$\tilde E_{\hat\varphi}=\boldsymbol{F}(\tilde{\boldsymbol{e}}_{(\hat\varphi)},\tilde{\boldsymbol{e}}_{(\hat t)})=\frac{1}{\rho_{\rm w}}F_{\varphi t}=\frac{1}{\sqrt{\Delta}\sin\theta}F_{\varphi t}, \tag{A11}$$

$$\tilde B_{\hat r}={}^*\boldsymbol{F}(\tilde{\boldsymbol{e}}_{(\hat t)},\tilde{\boldsymbol{e}}_{(\hat r)})=F_{\hat\theta\hat\varphi}=\frac{1}{\sqrt{\Sigma g_{\varphi\varphi}}}F_{\theta\varphi}, \tag{A12}$$

$$\tilde{B}_{\hat{\theta}} = {}^{*}\boldsymbol{F}(\tilde{\boldsymbol{e}}_{(\hat{t})}, \tilde{\boldsymbol{e}}_{(\hat{\theta})}) = -F_{\hat{r}\hat{\varphi}} = \frac{\sqrt{\Delta}}{\sqrt{\Sigma g_{\varphi\varphi}}} F_{\varphi r}, \tag{A13}$$

$$\tilde{B}_{\hat{\varphi}} = {}^{*}\boldsymbol{F}(\tilde{\boldsymbol{e}}_{(\hat{t})}, \tilde{\boldsymbol{e}}_{(\hat{\varphi})}) = \sqrt{g_{rr} g_{\theta\theta}} F^{r\theta} = \frac{\Sigma}{\sqrt{\Delta}} F^{r\theta}, \tag{A14}$$

where ${}^{*}\boldsymbol{F}$ refers to the Maxwell tensor, which is the dual of the Faraday tensor $\boldsymbol{F}$. For example, Figure 2 depicts the distribution of Equations (A12) and (A13) on the poloidal plane. We could use Equations (A4) and (A5) to compute $J^{\hat{r}}$ and $J^{\hat{\theta}}$, which are depicted in Figures 8 and 9. However, in actual calculations, we compute J^{r} and J^{θ} from Equations (47) and (48) and convert them into the ZAMO-measured quantities using the transformation law of the one-form bases that are dual to the ZAMO's tetrad, Equations (4)–(7).

Appendix B
Stationary Vacuum Magnetosphere

In this appendix, we formulate the basic equations to solve the initial stationary electromagnetic fields.

B.1. Gauss's Law

The inhomogeneous part of the Maxwell equations can be written as

$$\nabla_{\mu} F^{\nu\mu} = \frac{4\pi}{c} J^{\nu}, \tag{B1}$$

where ∇_{μ} denotes the covariant derivative with respect to the coordinate variable x^{μ}, $F^{\nu\mu}$ is the electromagnetic field strength tensor, and J^{ν} is the four current density. Putting $\nu = 0$, we obtain Gauss's law,

$$\frac{1}{\sqrt{-g}} \partial_{\mu} (\sqrt{-g} F^{0\mu}) = 4\pi\rho, \tag{B2}$$

where ρ refers to the electric charge density, and $\sqrt{-g} = \Sigma \sin\theta$. In the Kerr spacetime, we obtain

$$F^{01} = F^{tr} = \frac{g^{rr}}{{\rho_{\rm w}}^2} (-g_{\varphi\varphi} F_{tr} + g_{t\varphi} F_{\varphi r}), \tag{B3}$$

$$F^{02} = F^{t\theta} = \frac{g^{\theta\theta}}{{\rho_{\rm w}}^2} (-g_{\varphi\varphi} F_{t\theta} + g_{t\varphi} F_{\varphi\theta}), \tag{B4}$$

$$F^{03} = F^{t\varphi} = \frac{1}{{\rho_{\rm w}}^2} F_{\varphi t}. \tag{B5}$$

At $t = 0$, we assume a stationary and axisymmetric magnetosphere, $\partial_t = \partial_{\varphi} = 0$, to obtain

$$F_{rt} = A_{t,r} - A_{r,t} = A_{t,r} = \partial_r A_t, \tag{B6}$$

$$F_{\theta t} = A_{t,\theta} - A_{\theta,t} = A_{t,\theta} = \partial_{\theta} A_t, \tag{B7}$$

$$F_{\varphi t} = A_{t,\varphi} - A_{\varphi,t} = 0, \tag{B8}$$

$$F_{\varphi r} = A_{r,\varphi} - A_{\varphi,r} = -\partial_r A_{\varphi}, \tag{B9}$$

$$F_{\theta\varphi} = A_{\varphi,\theta} - A_{\theta,\varphi} = \partial_{\theta} A_{\varphi}, \tag{B10}$$

where $A_{\mu} = (A_t, A_r, A_{\theta}, A_{\varphi})$ denotes the vector potential; $F_{\mu\nu} = \partial_{\mu} A_{\nu} - \partial_{\nu} A_{\mu}$. Note that $F_{r\theta,\varphi} + F_{\theta\varphi,r} + F_{\varphi r,\theta} = 0$ (i.e., $\nabla \boldsymbol{B} = 0$) is automatically satisfied.

For an observer whose four velocity is u^{ν}, the electromagnetic field components are given by

$$E_{\mu} = F_{\mu\nu} u^{\nu} \tag{B11}$$

and

$$B^{\mu} = \frac{1}{2} \eta_{\nu}{}^{\mu\rho\sigma} F_{\rho\sigma} u^{\nu}, \tag{B12}$$

where the completely antisymmetric Levi–Civita tensor density is defined by

$$\begin{aligned} \eta_{\nu\mu\rho\sigma} &= -\eta_{\mu\nu\rho\sigma} = -\eta_{\rho\mu\nu\sigma} = -\eta_{\sigma\mu\rho\nu} \\ &= -\eta_{\nu\rho\mu\sigma} = -\eta_{\nu\sigma\rho\mu} = -\eta_{\nu\mu\sigma\rho} \end{aligned} \tag{B13}$$

and

$$\eta_{tr\theta\varphi} = -\frac{1}{\eta^{tr\theta\varphi}} = \sqrt{-g}. \tag{B14}$$

Thus, for a distant static observer whose four velocity is $\xi^{\mu} = (1, 0, 0, 0)$, that is, the time-like Killing vector, the electric field components are obtained by

$$E_r = F_{rt}, \quad E_{\theta} = F_{\theta t}, \quad E_{\varphi} = F_{\varphi t} \tag{B15}$$

in the Boyer–Lindquist coordinate. The magnetic field becomes

$$\begin{aligned} B^r &= \frac{-g_{tt} F_{\theta\varphi} + g_{t\varphi} F_{\theta t}}{\sqrt{-g}}, \\ B^{\theta} &= \frac{-g_{tt} F_{\varphi r} + g_{t\varphi} F_{rt}}{\sqrt{-g}}, \\ B_{\varphi} &= -\sqrt{-g} F^{r\theta}. \end{aligned} \tag{B16}$$

Substituting Equations (B6), (B7), (B9), and (B10) into Equation (B2), we obtain Gauss's law:

$$\begin{aligned} &\frac{1}{\Sigma} \frac{\partial}{\partial r} \left(\frac{A}{\Sigma} \frac{\partial A_t}{\partial r} \right) + \frac{1}{\Delta \Sigma \sin\theta} \frac{\partial}{\partial \theta} \\ &\quad \times \left(\frac{A}{\Sigma} \sin\theta \frac{\partial A_t}{\partial \theta} \right) + \frac{1}{\Sigma} \frac{\partial}{\partial r} \left(\frac{2Mar}{\Sigma} \frac{\partial A_{\varphi}}{\partial r} \right) \\ &\quad + \frac{1}{\Delta \Sigma \sin\theta} \frac{\partial}{\partial \theta} \left(\frac{2Mar}{\Sigma} \sin\theta \frac{\partial A_{\varphi}}{\partial \theta} \right) = 4\pi\rho. \end{aligned} \tag{B17}$$

It follows that this Poisson equation contains only A_t (i.e., the scalar potential) if the BH is nonrotating (i.e., $a = 0$). However, around a rotating BH (i.e., if $a \neq 0$), A_{φ} comes into Gauss's law. We thus need one more differential equation that contains both A_t and A_{φ}.

B.2. The Biot–Savart Law

To obtain an independent constraint on A_t and A_{φ}, we consider the Biot–Savart law. Putting $\nu = \varphi$ in Equation (B1), we obtain

$$\frac{1}{\sqrt{-g}} \partial_{\mu} (\sqrt{-g} F^{\varphi\mu}) = \frac{4\pi}{c} J^{\varphi}. \tag{B18}$$

Thus, Equations (B3)–(B10) give

$$-\frac{1}{\sin\theta}\frac{\partial}{\partial r}\left(\frac{\Delta - a^2\sin^2\theta}{\Sigma}\frac{\partial A_\varphi}{\partial r}\right) - \frac{1}{\Delta}\frac{\partial}{\partial\theta} \times \left(\frac{\Delta - a^2\sin^2\theta}{\Sigma\sin\theta}\frac{\partial A_\varphi}{\partial\theta}\right) + \frac{\partial}{\partial r}\left(\frac{2Mar\sin\theta}{\Sigma}\frac{\partial A_t}{\partial r}\right) + \frac{1}{\Delta}\frac{\partial}{\partial\theta}\left(\frac{2Mar\sin\theta}{\Sigma}\frac{\partial A_t}{\partial\theta}\right) = 4\pi\Sigma\sin\theta J^\varphi, \tag{B19}$$

where $c = 1$ is used. It follows that this equation contains only A_φ (i.e., the azimuthal component of the vector potential) if $a = 0$. However, if $a \neq 0$, we must simultaneously solve the two second-order partial differential Equations (B17) and (B19) for A_t and A_φ.

It should be noted that the coefficients of the $\partial_r^2 A_\varphi$ and $\partial_\theta^2 A_\varphi$ terms in Equation (B19) change sign at the static limit, where g_{tt} vanishes. Since the coefficients of these two highest-order derivative terms change sign with respect to those of the other two highest-order derivative terms (i.e., the $\partial_r^2 A_t$ and $\partial_\theta^2 A_t$ terms), the solution diverges during iterations from the inside of the static limit (i.e., within the so-called "ergosphere") if we impose boundary conditions in the same way as standard elliptic-type partial differential equations. This ill behavior is incurred because a static observer (with respect to the star) becomes unphysical within the ergosphere.

There are many ways to overcome this ill behavior. In the present paper, we solve this issue by adopting the ZAMO as a physical observer. Using the ZAMO's tetrad, Equations (4)–(7), we can replace A_t with the ZAMO-measured scalar potential, $A_{\hat{t}}$ (Equation (12)), and obtain the two elliptic-type Equations (14) and (19), which describe the initial electromagnetic fields at $t = 0$.

Appendix C
Pair Production Rate

Using the self-similar analytical solution of the Newtonian ADAF model (Mahadevan 1997), we find that the photons are emitted at the rate

$$q_{\rm ff} = 1.8 \times 10^2 \theta_{\rm e} \dot{m}^2 M_9^{-2}\left(\frac{r}{2M}\right)^{-3} \ {\rm erg\ s^{-1}\ cm^{-3}} \tag{C1}$$

by bremsstrahlung, where $\theta_{\rm e} \equiv kT_{\rm e}/m_{\rm e}c^2$ denotes the dimensionless electron temperature. The luminosity of this bremsstrahlung emission can be computed as

$$L_{\rm ff}(r) = 2\pi\int_{\theta_1}^{\theta_2}\int_{r_{\rm min}}^{r} q_{\rm ff}(r) r^2\sin\theta dr d\theta \approx 2\pi \times 1.8 \times 10^2\theta_{\rm e}\dot{m}^2 M_9^{-2}(2M)^3\ln\left(\frac{r}{2M}\right), \tag{C2}$$

where $\theta_1 \sim 60^\circ$ and $\theta_2 \sim 120^\circ$ denote the upper and lower boundary colatitudes of the ADAF.

In general, if one photon species (e.g., ADAF bremsstrahlung photons or gap-emitted gamma rays) collides with another photon species (e.g., ADAF bremsstrahlung photons or ADAF synchrotron photons), the pair production rate is given by

$$\dot{n}_\pm(r) = \int d\nu_\gamma \alpha_{\gamma\gamma}\frac{1}{c}\int\frac{I_\nu}{h\nu}d\Omega_\gamma, \tag{C3}$$

where $d\Omega_\gamma$ refers to the photon propagation solid angle,

$$\alpha_{\gamma\gamma} = (1-\mu)\int_{\epsilon_{\rm th}}^{\infty}\frac{dF_\gamma}{d\epsilon_\gamma}\sigma_{\gamma\gamma}d\epsilon_\gamma \approx (1-\mu)F_\gamma\sigma_{\gamma\gamma} \tag{C4}$$

denotes the photon–photon absorption coefficient, and

$$F_\gamma \equiv \int d\nu_\gamma \int\frac{I_\nu}{h\nu}d\Omega_\gamma \tag{C5}$$

denotes the photon number flux; I_ν, ν_γ, and μ show the specific intensity, photon frequency, and cosine of the photon collision angles, respectively.

In the present case, the two species are the same ADAF bremsstrahlung photons. Thus, we obtain

$$\dot{n}_\pm(r) \approx (1-\mu)\sigma_{\gamma\gamma}\frac{{F_\gamma}^2}{c}. \tag{C6}$$

Evaluating the flux with the luminosity by

$$F_\gamma(r) \approx \frac{L_{\rm ff}(r)}{2\pi r^2\epsilon_\gamma}, \tag{C7}$$

where the photon energy can be estimated to be $\epsilon_\gamma \approx 3\theta_{\rm e}m_{\rm e}c^2$, and assuming that the pair production rate is uniform within $r < 4M$, we obtain Equation (51), where the relative velocity factor is evaluated as $1-\mu = 0.2$, and the pair production cross section is 20% of the Thomson cross section, $\sigma_{\gamma\gamma} = 0.2\sigma_{\rm T}$.

Appendix D
Covariance of the Radiation-reaction Force

We explain here that the radiation-reaction force contains not only those obtained in a flat space (Cerutti et al. 2012, 2013),

$$P_{\rm rad,flat} = \frac{2}{3}e^2 c\frac{q^2}{m^2}\gamma^2\left[-\left(\frac{\boldsymbol{v}}{c}\cdot\tilde{\boldsymbol{E}}\right)^2 + \left(\tilde{\boldsymbol{E}} + \frac{\boldsymbol{v}}{c}\times\tilde{\boldsymbol{B}}\right)^2\right], \tag{D1}$$

in locally homogeneous $\tilde{\boldsymbol{E}}$ and $\tilde{\boldsymbol{B}}$ fields but also the power of radiative processes that result from any kind of acceleration. To find this, we write down Equation (44) in a covariant form,

$$\frac{du^\mu}{d\lambda} = -\Gamma^\mu{}_{\rho\sigma}u^\rho u^\sigma + \frac{q}{m}F^\mu{}_\rho u^\rho, \tag{D2}$$

where the friction term is dropped on the right-hand side to draw the conclusion from the first principles. Both the inertial (e.g., the centrifugal and Coriolis forces) and gravitational (due to the spacetime curvature) forces are included in the connection coefficients, $\Gamma^\mu_{\rho\sigma}$. For example, when a charge (or its guiding center) moves along a curved magnetic field line in a flat space, we can introduce a local cylindrical (or polar) coordinate system whose origin resides at the center of the curved path of 3D particle motion. In this coordinate, the $\Gamma^\mu_{\rho\sigma}u^\rho u^\sigma$ term gives the centripetal acceleration, $a_\perp = c^2/R_{\rm c}$, where $R_{\rm c}$ refers to the curvature radius of the 3D particle motion. Since Equation (46) is covariant, the effect of such curvature radiation is included in any frame of reference. Accordingly, we can take into account the radiation effects due to any acceleration. Note that a charged particle does radiate by gravitational acceleration, irrespective of the frame of reference.

In the actual program, we can compute the radiation-reaction force $F^j_{\rm rad}$ iteratively as follows.

(1) We first set $F^j_{\rm rad}=0$ and update $du^j/d\lambda$ and $du^0/d\lambda=\gamma$ by Equation (44).

(2) Second, we substitute the solved u^μ in Equation (46) to update $F^j_{\rm rad}$.

(3) Third, we use the updated $F^j_{\rm rad}$ and solve Equation (44) for u^μ again.

(4) We iterate steps 2 and 3 until $F^j_{\rm rad}$ saturates. If we use the $F^j_{\rm rad}$ obtained in the previous step for each particle and start from step 3, the number of iterations can be reduced.

Appendix E
Discretization of Basic Equations

We discretize the Maxwell Equations (35)–(37) by adopting the Yee lattice. Electric field components, E and D, are evaluated at half-integer time steps, e.g., $t\pm(1/2)\Delta_t$, and the magnetic field component, B, is evaluated at integer time steps at time $t+\Delta_t$. Accordingly, Equations (35)–(37) are discretized as follows:

$$\begin{aligned}&{B^{n+1}}_{i+1/2,j+1/2}-{B^{n}}_{i+1/2,j+1/2}\\&=-c_1\nu_x({E^{n+1/2}}_{i+1,j+1/2}-{E^{n+1/2}}_{i,j+1/2})\\&\quad+c_2\nu_y({D^{n+1/2}}_{i+1/2,j+1}-{D^{n+1/2}}_{i+1/2,j}),\end{aligned}\tag{E1}$$

$$\begin{aligned}&{D^{n+1/2}}_{i+1/2,j}-{D^{n-1/2}}_{i+1/2,j}\\&=c_3\nu_y({B^{n}}_{i+1/2,j+1/2}-{B^{n}}_{i+1/2,j-1/2})\\&\quad-4\pi(\Delta_t)\frac{\Sigma^2}{A}\bigg|_{i+1/2,j}(J^r)^n_{i+1/2,j},\end{aligned}\tag{E2}$$

$$\begin{aligned}&{E^{n+1/2}}_{i,j+1/2}-{E^{n-1/2}}_{i,j+1/2}\\&=-c_4\nu_x({B^{n}}_{i+1/2,j+1/2}-{B^{n}}_{i-1/2,j+1/2})\\&\quad-4\pi(\Delta_t)\frac{\Sigma^2\Delta\sin\theta}{A}\bigg|_{i+1/2,j}(J^\theta)^n_{i,j+1/2},\end{aligned}\tag{E3}$$

where the super- and subscripts denote the temporal and spatial labels, respectively, and the Courant numbers are defined by

$$\nu_x\equiv\frac{\Delta_t}{\Delta_x},\tag{E4}$$

$$\nu_y\equiv\frac{\Delta_t}{\Delta_y}.\tag{E5}$$

Here Δ_t denotes the time step, Δ_x denotes the constant interval of the radial tortoise coordinate, and $\Delta_y=\sin\theta\Delta_\theta$ denotes the constant azimuthal grid interval. Denoting the inner and outer boundary positions as ${r_*}^{\rm min}$ and ${r_*}^{\rm max}$, we obtain $\Delta_x=({r_*}^{\rm max}-{r_*}^{\rm min})/(N_x-1)$, where N_x denotes the number of radial grids. Since we consider the colatitude range $0<1-\cos\theta<2$, we obtain $\Delta_y=2/(N_y-1)$, where N_y denotes the number of meridional grids.

As for the Hamilton–Jacobi Equations (44) and (47)–(49), we evaluate the particle position (r, θ, φ) at half-integer time steps and the momentum (u^r, u^θ, u^φ, and γ) at integer time steps. Namely, particle's momentum evolves by (Equation (44))

$$\boldsymbol{u}^{n+1}-\boldsymbol{u}^n=(\Delta_t)\boldsymbol{F}(t^{n+1/2},\boldsymbol{x}^{n+1/2},\boldsymbol{u}^{n+1/2}),\tag{E6}$$

where F_i represents the right-hand side of Equation (44).

On the other hand, particle's position evolves by (Equations (47)–(49))

$$r^{n+1/2}=r^{n-1/2}+\left(\frac{u^r}{u^t}\right)^n,\tag{E7}$$

$$\theta^{n+1/2}=\theta^{n-1/2}+\left(\frac{u^\theta}{u^t}\right)^n,\tag{E8}$$

$$\varphi^{n+1/2}=\varphi^{n-1/2}+\left(\frac{u^\varphi}{u^t}\right)^n.\tag{E9}$$

The Boyer–Lindquist radial coordinate r can be readily converted into $x=r_*$ by Equation (10), whereas θ is related to y by $y=1-\cos\theta$.

To find the initial stationary solution, we divide the tortoise coordinate x uniformly in the range $-15.8180<x<20.0000$ and the meridional coordinate y uniformly in the range $0<y=1-\cos\theta<2$. Accordingly, the Boyer–Lindquist coordinates are divided nonuniformly as $r_1=1.4651M$, $r_2=1.4656M$, $r_3=1.4662M$, …, $r_{599}=19.9462M$, $r_{600}=20.0000M$, and $\theta_1=0^\circ$, $\theta_2=2.^\circ6160$, $\theta_3=3.^\circ7000$, $\theta=4.^\circ5319$, …, $\theta_{959}=89.^\circ9104$, $\theta_{960}=89.^\circ9701$, $\theta_{961}=90.^\circ0298$, …, $\theta_{1918}=(180.0000-3.7000)^\circ$, $\theta_{1919}=(180.0000-2.6160)^\circ$, $\theta_{1920}=180.^\circ0000$.

To perform PIC simulations, we must make the radial range small compared to the stationary case, because the Gauss and Biot–Savart laws are solved for the toroidal current distribution within $r<20M$, which typically makes the solved poloidal electromagnetic fields accurate only within $r<14M$. The actual value of the right-hand side (i.e., $14M$ in this case) depends on the r dependence of $J^\varphi_{\rm eq}$. For a split-monopole case, $J^\varphi_{\rm eq}\propto r^{-4}$, or a paraboloidal case, $J^\varphi_{\rm eq}\propto r^{-3}$, the outer radial boundary of $r\sim14M$ is conservatively justified. For PIC simulations, we thus adopt the inner 960 points to restrict the simulation range within $x_1=-15.8180<x<x_{960}=12.8244$ or, equivalently, $r_1=1.4646M<r<r_{960}=13.6854M$. For the meridional coordinate y, we adopt the same gridding as in the stationary case. We checked that the results change little when we halve the resolution either in the radial or meridional direction or when we halve the creation rate $1/k_{\rm create}$ (and hence the number of particles per cell).

Appendix F
Current Deposit

In our present 2D PIC simulations, we adopt a grid consisting of rectangles of unit size and place on it unit rectangular charges, where each unit rectangle grid cell has an area $\Delta_x\Delta_y$ (Appendix E). The total number of charges is assumed to be uniformly distributed over its 2D surface. As a charge moves, each grid cell boundary sweeps a fraction of the particle's unit area surface, getting the electric current flowing across the boundary. Using this "area weighting" (Villasenor & Buneman 1992), we sum up the currents carried by individual particles on each grid boundary.

We should note here that we take account of the particle motion only in the poloidal plane when we compute the current density, although the particles' EOM is solved three-dimensionally. Thus, we cannot compute the toroidal current density, J^φ, in our area-weighting method. It follows that the time evolution of E_φ cannot be solved from Ampere's law. Accordingly, the evolution of B^r or B^θ cannot be solved either, because the r and θ components of the Faraday law contain $\partial_\theta E_\varphi$ and $\partial_r E_\varphi$,

respectively. Thus, we are only able to solve the three components (i.e., B, D, and E) of the electromagnetic field with Equations (35)–(37) in the present 2D scheme, unless J^{φ} is constructed from the particle's toroidal motion by a "volume-weighting" method, which is outside the scope of the present paper.

ORCID iDs

Kouichi Hirotani https://orcid.org/0000-0002-2472-9002
Ruben Krasnopolsky https://orcid.org/0000-0001-5557-5387
Hsien Shang (尚賢) https://orcid.org/0000-0001-8385-9838
Ken-ichi Nishikawa https://orcid.org/0000-0001-6031-7040
Michael Watson https://orcid.org/0000-0001-5783-0513

References

Asada, K., & Nakamura, M. 2012, ApJL, 745, L28
Asada, K., Nakamura, M., & Pu, H.-Y. 2016, ApJ, 833, 56
Bacchini, F., Ripperda, B., Chen, A. Y., & Sironi, L. 2018, ApJS, 237, 6
Bardeen, J. M. 1970, Natur, 226, 64
Beskin, V. S., Istomin, Y. N., & Parev, V. I. 1992, SvA, 36, 642
Biretta, J. A., Sparks, W. B., & Macchetto, F. 1999, ApJ, 520, 621
Blandford, R. D., & Znajek, R. L. 1977, MNRAS, 179, 433
Bohdan, A., Niemiec, J., Pohl, M., et al. 2019, ApJ, 885, 10
Boyer, R. H., & Lindquist, R. W. 1967, JMP, 8, 265
Camenzind, M. 1986, A&A, 162, 32
Cerutti, B., Uzdensky, D. A., & Begelman, M. C. 2012, ApJ, 746, 148
Cerutti, B., Werner, G. R., Uzdensky, D. A., & Begelman, M. C. 2013, ApJ, 770, 147
Chen, A. Y., & Yuan, Y. 2020, ApJ, 895, 121
Chen, A. Y., Yuan, Y., & Yang, H. 2018, ApJL, 863, L31
Crinquand, B., Cerutti, B., Philippov, A. e., Parfrey, K., & Dubus, G. 2020, PhRvL, 124, 145101
Event Horizon Telescope Collaboration, Akiyama, K., Alberdi, A., et al. 2019, ApJL, 875, L5
Ferrarese, L., Ford, H. C., & Jaffe, W. 1996, ApJ, 470, 444
Hada, K., Doi, A., Kino, M., et al. 2011, Natur, 477, 185
Hada, K., Kino, M., Doi, A., et al. 2013, ApJ, 775, 70
Hada, K., Kino, M., Doi, A., et al. 2016, ApJ, 817, 131
Hirose, S., Krolik, J. H., De Villiers, J.-P., & Hawley, J. F. 2004, ApJ, 606, 1083
Hirotani, K., & Okamoto, I. 1998, ApJ, 497, 563
Hirotani, K., & Pu, H.-Y. 2016, ApJ, 818, 50
Hirotani, K., Pu, H.-Y., Lin, L. C.-C., et al. 2016, ApJ, 833, 142
Hughes, S. A., Keeton, C. R. I., Walker, P., et al. 1994, PhRvD, 49, 4004
Ichimaru, S. 1977, ApJ, 214, 840
Jackson, J. D. 1962, Classical Electrodynamics (New York: Wiley & Sons)
Junor, W., Biretta, J. A., & Livio, M. 1999, Natur, 401, 891
Kisaka, S., Levinson, A., & Toma, K. 2020, ApJ, 902, 80
Koide, S., Shibata, K., Kudoh, T., & Meier, D. L. 2002, Sci, 295, 1688
Kormendy, J., & Ho, L. C. 2013, ARA&A, 51, 511
Kovalev, Y. Y., Lister, M. L., Homan, D. C., & Kellermann, K. I. 2007, ApJL, 668, L27
Larkin, A. C., & McLaughlin, D. E. 2016, MNRAS, 462, 1864
Levinson, A., & Cerutti, B. 2018, A&A, 616, A184
Levinson, A., & Rieger, F. 2011, ApJ, 730, 123
Ly, C., Walker, R. C., & Junor, W. 2007, ApJ, 660, 200
Mahadevan, R. 1997, ApJ, 477, 585
McKinney, J. C., & Narayan, R. 2007, MNRAS, 375, 513
McKinney, J. C., Tchekhovskoy, A., & Blandford, R. D. 2012, MNRAS, 423, 3083
Mertens, F., Lobanov, A. P., Walker, R. C., & Hardee, P. E. 2016, A&A, 595, A54
Nakamura, M., & Asada, K. 2013, ApJ, 775, 118
Nakamura, M., Asada, K., Hada, K., et al. 2018, ApJ, 868, 146
Nakamura, M., & Meier, D. L. 2014, ApJ, 785, 152
Narayan, R., & Yi, I. 1994, ApJL, 428, L13
Neronov, A., & Aharonian, F. A. 2007, ApJ, 671, 85
Parfrey, K., Philippov, A., & Cerutti, B. 2019, PhRvL, 122, 035101
Perlman, E. S., Adams, S. C., Cara, M., et al. 2011, ApJ, 743, 119
Tanabe, K., & Nagataki, S. 2008, PhRvD, 78, 024004
Tchekhovskoy, A., Narayan, R., & McKinney, J. C. 2010, ApJ, 711, 50
Thorne, K. S., & MacDonald, D. 1982, MNRAS, 198, 339
Villasenor, J., & Buneman, O. 1992, CoPhC, 69, 306
Walker, R. C., Hardee, P. E., Davies, F. B., Ly, C., & Junor, W. 2018, ApJ, 855, 128
Wang, C.-C., & Zhou, H.-Y. 2009, MNRAS, 395, 301
Yuan, F., & Narayan, R. 2014, ARA&A, 52, 529